remote sensing

MDPI

Article

Spatiotemporal Variations in Biophysical Water Quality Parameters: An Integrated In Situ and Remote Sensing Analysis of an Urban Lake in Chile

Santiago Yépez [1,*], Germán Velásquez [2,3], Daniel Torres [1,4], Rodrigo Saavedra-Passache [5], Martin Pincheira [6], Hayleen Cid [7], Lien Rodríguez-López [8], Angela Contreras [9], Frédéric Frappart [10], Jordi Cristóbal [11], Xavier Pons [12], Neftali Flores [1] and Luc Bourrel [3]

1 Departamento Manejo de Bosques y Medio Ambiente, Facultad de Ciencias Forestales, Universidad de Concepción, Concepción 4070386, Chile; datorres2017@udec.cl (D.T.); neflores@udec.cl (N.F.)
2 Instituto de Geología Económica Aplicada, Universidad de Concepción, Concepción 4070386, Chile; germanvelasquez@udec.cl
3 UMR 5563 Géosciences Environnement Toulouse, Université de Toulouse, CNRS-IRD-OMP-CNES, 31000 Toulouse, France; luc.bourrel@ird.fr
4 Programa de Máster en Ingeniería de Montes, E.T.S.I Escuela Técnica Superior de Ingeniería, Universidad de Huelva, 21071 Huelva, Spain
5 Doctoral Program in Advanced Forestry Engineering, E.T.S.I Montes, Forestal y Medio Natural, Universidad Politecnica de Madrid—UPM, 28040 Madrid, Spain; rodrigo.saavedra@alumnos.upm.es
6 Forestal ARAUCO S.A., Gerencia de Planificación y Mejora Continua, Concepción 4030000, Chile; martin.pincheira@arauco.com
7 Departamento de Geofísica, Facultad de Ciencias Físicas y Matemáticas, Universidad de Concepción, Concepción 4070386, Chile; hayleencid2016@udec.cl
8 Facultad de Ingeniería, Arquitectura y Diseño, Universidad San Sebastián, Lientur 1457, Concepción 4030000, Chile; lien.rodriguez@uss.cl
9 Departamento Ciencias de la Tierra, Ciencias Químicas, Universidad de Concepción, Concepción 4030000, Chile; acontreras2016@udec.cl
10 ISPA, INRAE, Bordeaux Sciences Agro, 33140 Villenave d'Ornon, France; frederic.frappart@inrae.fr
11 Efficient Use of Water in Agriculture Program, Institute of Agrifood Research and Technology, Fruitcentre, Parc Científic i Tecnològic Agroalimentari de Lleida 23, 25003 Lleida, Spain; jordi.cristobal@irta.cat
12 Grumets Research Group, Departament de Geografia, Edifici B. Universitat Autònoma de Barcelona, 08193 Bellaterra, Catalonia, Spain; xavier.pons@uab.cat
* Correspondence: syepez@udec.cl; Tel.: +56-974511119

check for updates

Citation: Yépez, S.; Velásquez, G.; Torres, D.; Saavedra-Passache, R.; Pincheira, M.; Cid, H.; Rodríguez-López, L.; Contreras, A.; Frappart, F.; Cristóbal, J.; et al. Spatiotemporal Variations in Biophysical Water Quality Parameters: An Integrated In Situ and Remote Sensing Analysis of an Urban Lake in Chile. *Remote Sens.* **2024**, *16*, 427. https://doi.org/10.3390/rs16020427

Academic Editor: Timo Balz

Received: 15 November 2023
Revised: 9 January 2024
Accepted: 20 January 2024
Published: 22 January 2024

Correction Statement: This article has been republished with a minor change. The change does not affect the scientific content of the article and further details are available within the backmatter of the website version of this article.

Abstract: This study aims to develop and implement a methodology for retrieving bio-optical parameters in a lagoon located in the Biobío region, South-Central Chile, by analyzing time series of Landsat-8 OLI satellite images. The bio-optical parameters, i.e., chlorophyll-a (Chl-a, in $mg \cdot m^{-3}$) and turbidity (in NTU) were measured in situ during a satellite overpass to minimize the impact of atmospheric distortions. To calibrate the satellite images, various atmospheric correction methods (including ACOLITE, C2RCC, iCOR, and LaSRC) were evaluated during the image preprocessing phase. Spectral signatures obtained from the scenes for each atmospheric correction method were then compared with spectral signatures acquired in situ on the water surface. In short, the ACOLITE model emerged as the best fit for the calibration process, reaching R^2 values of 0.88 and 0.79 for Chl-a and turbidity, respectively. This underlies the importance of using inversion models, when processing water surfaces, to mitigate errors due to aerosols and the sun-glint effect. Subsequently, reflectance data derived from the ACOLITE model were used to establish correlations between various spectral indices and the in situ data. The empirical retrieval models (based on band combinations) yielding superior performance, with higher R^2 values, were subjected to a rigorous statistical validation and optimization by applying a bootstrapping approach. From this process the green chlorophyll index (GCI) was selected as the optimal choice for constructing the Chl-a retrieval model, reaching an R^2 of 0.88, while the red + NIR spectral index achieved the highest R^2 value (0.79) for turbidity analysis, although in the last case, it was necessary to incorporate data from several seasons for an adequate model training. Our analysis covered a broad spectrum of dates, seasons, and years, which allowed us to search deeper into the evolution of the trophic state associated with the lake. We identified a

striking eight-year period (2014–2022) characterized by a decline in Chl-a concentration in the lake, possibly attributable to governmental measures in the region for the protection and conservation of the lake. Additionally, the OLI imagery showed a spatial pattern varying from higher Chl-a values in the northern zone compared to the southern zone, probably due to the heat island effect of the northern urban areas. The results of this study suggest a positive effect of recent local regulations and serve as the basis for the creation of a modern monitoring system that enhances traditional point-based methods, offering a holistic view of the ongoing processes within the lake.

Keywords: eutrophication; Landsat; Chl-a; turbidity; spectral signatures; OLI; Chile

1. Introduction

Lakes in urban areas contribute to the quality of life by providing ecological and social ecosystem services considered as benefits that people receive from the environment. These lakes represent intricate systems that ensure the continued provision of a range of ecosystem services that demand integrated actions within the surrounding watershed or directly within the lake itself [1,2], especially in urban lake environments. Ensuring the quality of surface and groundwater is an essential duty carried out by organizations responsible for water supply and management [3]. It is crucial to implement appropriate conservation and management measures, both conducing to improve the water quality of a lake, thus safeguarding their long-term ecological and socioeconomic value [4] by analyzing the trophic state of a lake. The trophic state of a lake indicates its level of biological productivity and water quality, which is determined by the availability of nutrients. Lakes can be classified into different trophic states, such as oligotrophic (low productivity), mesotrophic (moderate productivity) or eutrophic (high productivity) [5]. This state significantly influences the diversity and abundance of aquatic species, as well as the presence of algae and other organisms.

Regularly, to monitor water quality parameters (WQPs, i.e., Chl-a concentration and turbidity) a traditional point-based procedure is used, with sampling providing high-quality data. However, these data usually represent isolated sampling points and do not fully reflect a comprehensive spatial and temporal variations within the aquatic ecosystem [6]. To address challenges related to spatial and temporal coverage, remote sensing has been recognized as an optimal solution, leveraging advancements in sensors and methodologies. This has led to an extensive utilization of satellite technology in monitoring changes in freshwater bodies [7], allowing the observation and study of water quality at both regional and global scales [8]. Thus, remote sensing offers a comprehensive and immediate perspective of aquatic, atmospheric, and terrestrial systems, and it has significant advantages over traditional monitoring methods, including large-scale coverage, real-time monitoring capabilities, and cost-effectiveness. It serves as an optimal tool for the continuous monitoring of the water quality in surface bodies [9–11]. When this type of monitoring is also combined with in situ measurements, it can deliver unparalleled, cost-efficient, and quantitative assessments of water quality variations. This combination provides spatial resolutions reaching the scale of meters and a temporal frequency surpassing daily intervals [12].

Currently, there are several sources of remote sensing data for water quality studies such as the Terra/Aqua MODIS, Sentinel-2, or Landsat data, among others. However, one of the most important sources of remote sensing data is the Landsat archive. Since 1982 (Landsat-4 TM), this option enables the consistent monthly monitoring of inland water bodies, providing over 40 years of continuously recorded data at a suitable temporal frequency and spatial resolution. Particularly, Landsat-8 (L-8) Operational Land Imager (OLI) has a high radiometric resolution, a crucial parameter for recovering constituents, since water bodies act as dark objects and absorb a larger fraction of the downward

irradiance, resulting in a low signal-to-noise ratio (SNR) [13], and it has been successfully used to determine water quality data [14,15].

To monitor the water quality of a lake using satellite imagery, the chlorophyll-a (Chl-a—in $mg \cdot m^{-3}$) and turbidity (nephelometric turbidity units—NTU) arise as two essential apparent optical parameters (AOPs) for that purpose [16,17]. Chl-a is a parameter commonly used to assess the trophic state of coastal and inland waters due to its sensitivity and variation against many environmental factors. Chl-a is the green pigment found in aquatic plants, such as algae and cyanobacteria [18]. An increase in Chl-a concentration may indicate the proliferation of these organisms, often associated with eutrophication. The eutrophication process is defined as a natural phenomenon where excess nutrients in the water (such as nitrogen and phosphorus) promote the excessive growth of algae [19], which typically unfolds over thousands of years. Human activities can expedite this process, leading to the emergence of what is commonly referred as artificial or cultural eutrophication, triggering negative effects on water quality and the health of the aquatic ecosystem [20]. Additionally, elevated turbidity levels (NTU) can result in an opaque, hazy, or cloudy appearance of the water, which is closely related to suspended sediment concentrations [10,21].

Most of the studies carried out in "Laguna Grande San Pedro de La Paz" by remote sensing have been conducted by considering a fixed time scale. For example, Lilo-Saavedra et al. [22] have shown the accuracy of estimating representative water quality features in the lagoon using fused satellite images. Quintana-Sotomayor et al. [23] implemented an object-oriented classification methodology for multispectral images to quantify turbidity levels and generate a turbidity map of the lagoon. Rojas [24] focused its study on assessing the effects of land-use changes in the watershed of Laguna Grande on sedimentation rates. This was achieved through a multitemporal analysis using satellite imagery. Recently, Pedreros-Guarda et al. [25], implemented six automated methods for retrieving the surface water temperature of the lagoon using satellite thermal imagery.

According to the previous studies, our main objective was to develop spectral inversion models based on in situ data versus the reflectance signal to evaluate the possibility of estimating two of the most important WQPs for eutrophication dynamics monitoring, i.e., the Chl-a concentration and turbidity. Furthermore, these models play a key role in filling the spatial and temporal gaps in the analysis of historical data. The empirical retrieval models will facilitate the reconstruction of variable behaviors occurring when field data are not collected, thus increasing the robustness of the dataset. Our study encompasses the following key aspects: (i) the implementation of atmospheric correction methods to correct atmospheric distortions and the sun-glint effect in satellite data acquired from Landsat-8 OLI sensor; (ii) the development of an empirical retrieval model to quantify water quality parameters, specifically Chl-a and turbidity, including an assessment of statistical effectiveness; and (iii) the assessment of the spatial–temporal variability: it will allow us to understand the eutrophication processes during different seasonal conditions and multiple years.

2. Materials and Methods

2.1. Study Area

"Laguna Grande de San Pedro de la Paz" (Central-Southern Chile, Figure 1) is a shallow urban lake placed in the northwestern part of the Nahuelbuta mountain range (36°51′S, 73°06′W) at 220 m.a.s.l., in the southern margin of the Biobío River, approximately 5 km from the city of Concepción. It has a perimeter of 9800 m, a maximum length of 2675 m, and a maximum width of 1375 m. It covers an area of over 155 ha and reaches a maximum depth of 13.5 m, with an average depth of 8.1 m [26]. On its eastern side, Laguna Grande is bordered by a low-altitude mountain range of up to 360 m.a.s.l. This area is characterized by forest plantations, consisting of pine and eucalyptus trees (*Pinus radiata* and *Eucalyptus globulus*, respectively). Moreover, in the hills to the north, there has been a major urban and real estate development project in recent years. Laguna

Grande drains through the Los Batros estuary, receiving water from natural runoff as well as drainage from the surrounding residential areas [24]. The current trophic condition (using the trophic state index—TSI) of Laguna Grande de San Pedro has been categorized as mesotrophic (30 < TSI < 60), based on the Carlson [5] TSI classification and the data obtained by Urrutia et al. [27].

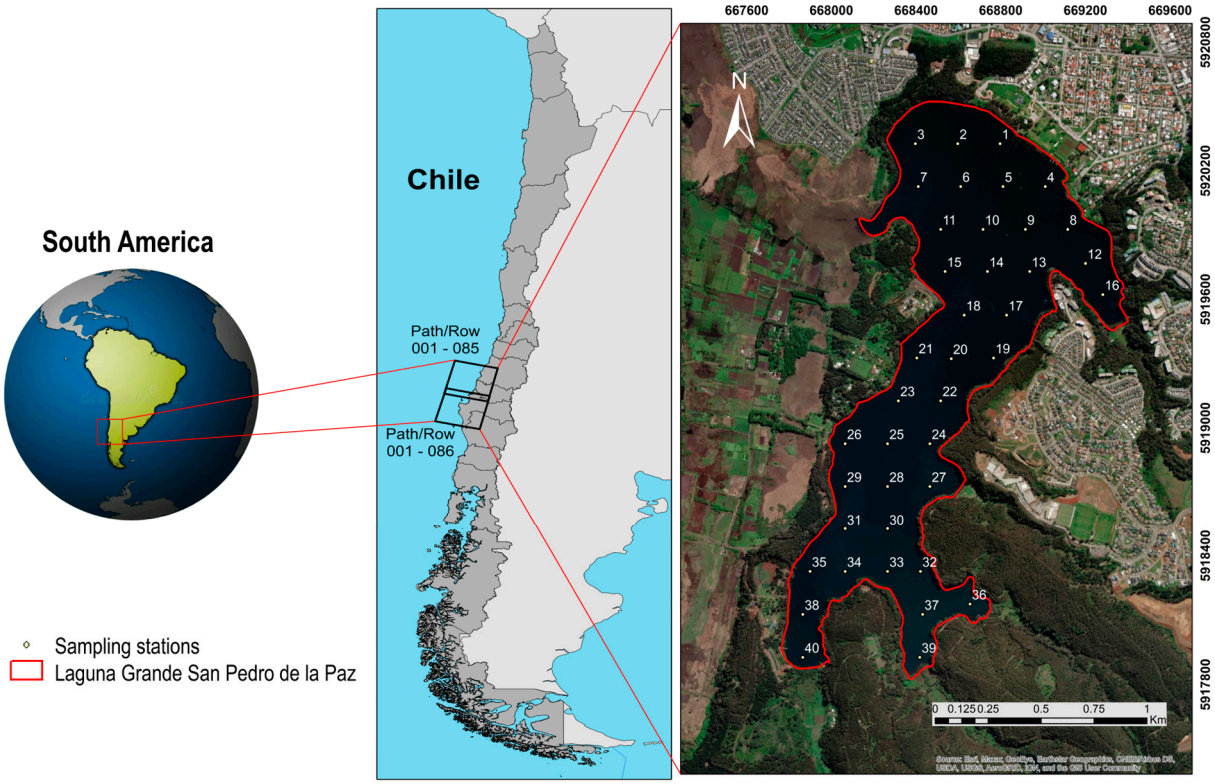

Figure 1. Location of "Laguna Grande San Pedro de la Paz", showing the distribution of the 40 surface sampling stations.

Over time, several external factors and natural causes have contributed to the deterioration of the lagoon's water quality. Primarily, this decline can be attributed to the occurrence of eutrophication processes. To comprehensively examine and analyze the water quality, a few decades ago, the "Dirección General de Aguas—DGA" (Water Agency of Chile) established three sampling stations within the lagoon (named as Sector Desagüe, Sector Centro, and Sector Sur). These stations facilitated the collection of traditional measurements, e.g., chlorophyll-a, turbidity, pH, CDOM, to assess the lagoon's water quality and its trophic condition. These three sampling stations operated from 1988 to 2013, but unfortunately these stations are no longer operational. Since 2014, sampling has been performed only at the Sector Centro 2 station, but the available information only includes three sampling missions by year between 2014 and 2016. Assuming four measurements per year, the percentage of missing data between 1988 and 2016, including all stations, is 28% [23].

2.2. Field Data of Water Parameters

For this project, three field surveys were conducted to collect surface water samples: (i) a first one in the spring season (24 October 2022); (ii) a second one in the summer season (6 January 2023); and (iii) the last one near to the fall season (1 March 2023). The selected dates were chosen to match with the schedule of L-8 satellite overflights over the lagoon. This selection aimed to align our field trips with the satellite's image acquisition dates, minimizing the time gap between an image capture and the sample collection.

To determine the location of sampling stations, a grid was performed, and forty (40) sampling points were distributed throughout the lake (Figure 1). Due to logistical constraints, we collected 40 samples in the summer field trip, 25 in the spring trip, and 20 in the fall trip, resulting in a total of 85 samples. These samples were collected using 1 L glass bottles, typically positioned approximately 20–30 cm below the water's surface. The samples were analyzed at the EULA-Chile Center laboratory and the results are summarized in Table 1. For the Chl-a analysis, the samples were subjected to filtration, extraction, and centrifugation, following the protocol of EPA method 445.0 described in the literature [28]. Subsequently, a fluorometric method was performed to measure Chl-a content, and unit transformations as well as parameter calculations were carried out using the corresponding calibration curve for the Turner Designs model 10-AU-005-CE equipment. With this process, Chl-a concentrations were obtained in milligrams per cubic meter ($mg \cdot m^{-3}$). For the turbidity determination, a specialized turbidimeter (2100Q Portable Turbidimeter Hach) was used to obtain the results in nephelometric turbidity units (NTU).

Table 1. Chl-a and turbidity concentrations obtained from the Laguna Grande water samples.

	24 October 2022 (40 Samples)		**6 January 2023 (25 Samples)**		**1 March 2023 (20 Samples)**	
Statistics	**Chl-a $mg \cdot m^{-3}$**	**Turbidity *NTU***	**Chl-a $mg \cdot m^{-3}$**	**Turbidity *NTU***	**Chl-a $mg \cdot m^{-3}$**	**Turbidity *NTU***
Mean	4.7	2.4	3.4	1.9	6.4	7.3
Standard Deviation	0.6	0.5	0.6	0.8	1.3	4.1
Max.	6.7	3.8	4.4	3.8	8.7	20.2
Min.	3.5	1.5	2.2	0.6	3.8	2.4

During the last field trip, further important water quality parameters were measured, such as: temperature (°C), dissolved oxygen ($mg \cdot L^{-1}$), oxygen saturation (%), conductivity ($mhos \cdot cm^{-1}$), and pH, which allowed us to know the trophic state of the lake from the quasi-synchronously measurements with the satellite overpass (Table 2).

Table 2. Values for temperature, dissolved oxygen, oxygen saturation, conductivity, and pH obtained from Laguna Grande.

	Temperature (C°)	**Dissolved Oxygen ($mg \cdot L^{-1}$)**	**Oxygen Saturation (%)**	**Conductivity ($mhos \cdot cm^{-1}$)**	**pH**
Mean	21.3	7.1	78.7	118.1	7.2
Min.	20.9	6.7	76.1	115.0	6.4
Max.	21.8	8.4	87.6	119.9	7.4
Standard deviation	0.3	0.5	2.9	1.1	0.3

2.3. Field Measurement of Water Spectral Signatures (R_{rs})

We performed reflectance (R_{rs}) measurements at 15 sampling stations using an ASD FieldSpec-4 spectroradiometer (ASD Inc., Falls Church, VA, USA, Malvern Panalytical, Malvern, UK). This instrument is specifically designed to operate within a wavelength ranging from 350 nm to 2500 nm.

The above-water remote sensing reflectance was calculated by Equation (1):

$$\mathrm{Rrs} = \frac{L_w(\lambda)}{E_d(\lambda)} \left(\mathrm{sr}^{-1}\right) \quad (1)$$

where R_{sr} represents the above-water remote sensing reflectance, $L_w(\lambda)$ denotes the spectral radiance of the target ($W \cdot cm^{-2} \cdot sr^{-1} \cdot \mu m^{-1}$), and $E_d(\lambda)$ refers to the spectral irradiance of the reference plate ($W \cdot cm^{-2} \cdot \mu m^{-1}$). A white reference panel was used to simulate a Lambertian surface. Measurements were made between 10:00 and 13:00, a time of optimal conditions with low solar tilt, high radiant energy, and favorable weather. Radiometric

measurements followed the methods established by Milton [29] and Mobley [30], performed under conditions of low wind (0–4 $m \cdot s^{-1}$), clear skies, and solar angles between 0° and 30°. To minimize the sun-glint effect, the spectroradiometer was positioned at an inclination of 40° with respect to the vertical and 135° from the sun. The sensor was placed 1 meter above the water surface. Ten repeated measurements were performed at each station, to verify the obtained data directly in the field. Some anomalous spectra caused by random solar flares were present in the measured result. However, these were suppressed, and the remaining spectra were averaged (Figure 2).

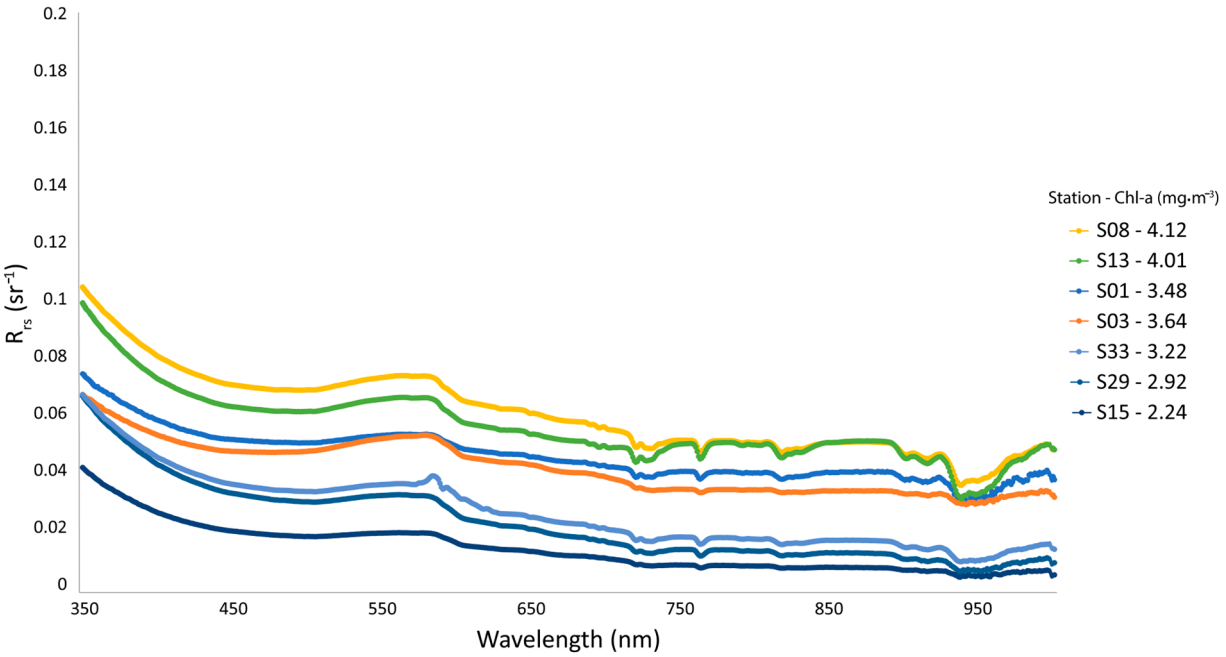

Figure 2. In situ measured R_{rs} spectra with their corresponding Chl-a value.

The ENVI-IDL 5.6 software was used to build a spectral library of surface water samples at different Chl-a concentrations. This spectral library of seven spectral profiles were used to evaluate the performance of the different atmospheric correction methods in the OLI L-8 sensor scenes.

2.4. Satellite Image Data and Atmospheric Correction Methods

2.4.1. Landsat-8 OLI Satellite Imagery

Laguna Grande is located at the intersection of two orbits, namely path/row combinations 001/085 and 001/086, resulting in a region of overlap which covers approximately 31 km. It must be noted that the satellite images used in this study were obtained from the official website of the United States Geological Survey (USGS), specifically from collection 2, levels 1 and 2. These images can be accessed through https://earthexplorer.usgs.gov (accessed on 15 June 2023).

Three satellite images from the L-8 OLI sensor (Table 3) were used to develop the empirical models for retrieving bio-optical parameters, i.e., Chl-a and turbidity. The empirical models were developed by a combination of the signal reflectance and in situ data. The time difference between in situ data collection and satellite image acquisition did not exceed 3 days. No rainfall events occurred during the whole data collection. Seven additional L-8 OLI images were used to study the spatiotemporal variability of bio-optical parameters (Chl-a and turbidity) in the lake during different seasonal conditions between hydrological cycles for 2014 and 2022.

Table 3. The three L-8 OLI satellite images used to develop the Chl-a and turbidity spectral retrieval models.

Image ID	In Situ Date	Image Date	Days	Path/Row
LC08_L1TP_001085_20221021_20221101_02_T1	24 October 2022	21 October 2022	±3	001/085
LC08_L1TP_001086_20230109_20230124_02_T1	6 January 2023	9 January 2023	±3	001/086
LC08_L1TP_001086_20230226_20230301_02_T1	1 March 2023	26 February 2023	±3	001/086

2.4.2. Atmospheric Correction Methods

A comparison of four different atmospheric correction (AC) methods designed to obtain surface water reflectance from L-8 OLI radiance images were applied and seven lake stations were used to compare the performance of these four atmospheric correction models:

(1) The first tested model was ACOLITE developed by RBINS (Royal Belgian Institute of Natural Sciences), commonly used to apply the AC on satellite images in applications related to inland and coastal waters. ACOLITE uses the approach known as dark spectrum adjustment to perform the atmospheric correction [31–35]. ACOLITE is designed to remove atmospheric influences, such as scattering and absorption, and to improve the accuracy of remote sensing data for different applications. It includes algorithms to detect and quantify sun-glint (specular reflection of sunlight on the water surface) in satellite imagery, which can introduce significant errors in remote sensing data, especially in coastal and oceanic regions. Once sun-glint is detected, ACOLITE applies correction algorithms to adjust pixel values to compensate for the overestimation of reflectance caused by the effect of the solar reflection. In this study, the v20210114.0 version was used.

(2) The second tested model was iCOR, developed by De Keukelaere et al. [36] to process satellite data acquired over coastal, inland, or transitional waters and land. iCOR employs the moderate-resolution atmospheric radiance and the transmittance model 5, known as MODTRAN5 [37], to perform radiative transfer calculations. In addition, it uses the look-up-table (LUT) mode to speed up retrieval processes. An important aspect of iCOR is its ability to identify whether a pixel belongs to a water or land area, allowing its application to a specific atmospheric correction [38]. The iCOR version used was v3.0 in the SNAP 8.0 software.

(3) The third model was the Land Surface Reflectance Code (LaSRC), developed by E. Vermote [39], National Aeronautics and Space Administration (NASA), Goddard Space Flight Center (GSFC) that was later modified by the USGS Earth Resources Observation and Science (EROS) center. The LaSRC model generates top-of-atmosphere reflectance (TOA) and top-of-atmosphere brightness temperature (BT) using calibration parameters provided in the metadata. Then, atmospheric correction routines are applied to the L-8 TOA reflectance data using additional information such as water vapor, ozone, and aerosol optical thickness (AOT) obtained from the Moderate Resolution Imaging Spectroradiometer (MODIS). In addition, the digital elevation model derived from the Earth Topography Five Minute Grid (ETOPO5) is used to generate surface reflectance [39]. This product can be downloaded from the USGS website (https://www.usgs.gov/landsat-missions/landsat-surface-reflectance; accessed on 15 June 2023). Finally, scaling Equation (2) was applied to normalize the reflectance values between 0 and 1 and hence to compare with the other methods.

$$\text{Rrs}(\lambda) = 0.0000275 \times \text{Pixel Value} - 0.2 \quad (2)$$

(4) The last method was C2RCC (Case 2 Regional CoastColour), which is based on a deep learning approach using a set of trained neural networks to simulate reflectance data in water bodies and radiances in the upper atmosphere. Its main outputs are associated with the inherent optical properties (IOPs) of water, i.e., those that depend exclusively on the absorption and scattering of its constituents [40]. This method considers three sets of neural networks for the calculation of reflectance depending

on the research objective: the C2RCC-Nets (standard neural network suggested for eutrophic or mesotrophic water bodies), the C2X-Nets (specialized neural networks applied to water bodies with high concentrations of suspended matter and chlorophyll concentration) and the C2X-COMPLEX-Nets (suggested mainly for use in inland waters) [41]. C2RCC can be used as a complement in the SNAP 8.0 software, and it allows the calculation of reflectance in Sentinel 3 OLCI, Sentinel 2 MSI, Landsat-8/9, MODIS and MERIS satellite images (e.g., [42,43]).

2.5. Methodology for Water Quality Modeling

To determine water quality parameters (Chl-a and turbidity) from in situ and satellite data (OLI L-8 images), we implemented a detailed workflow (Figure 3). Satellite images were empirically employed to estimate water quality parameters by identifying optimal spectral relationships with in situ data for the estimation of turbidity and Chl-a concentrations. Extracted values from satellite-derived spectral indices were systematically compared with in situ data through scatter plots. The primary goal was to establish a robust spectral inversion model, emphasizing the evaluation of the coefficient of determination for each combination of spectral indices.

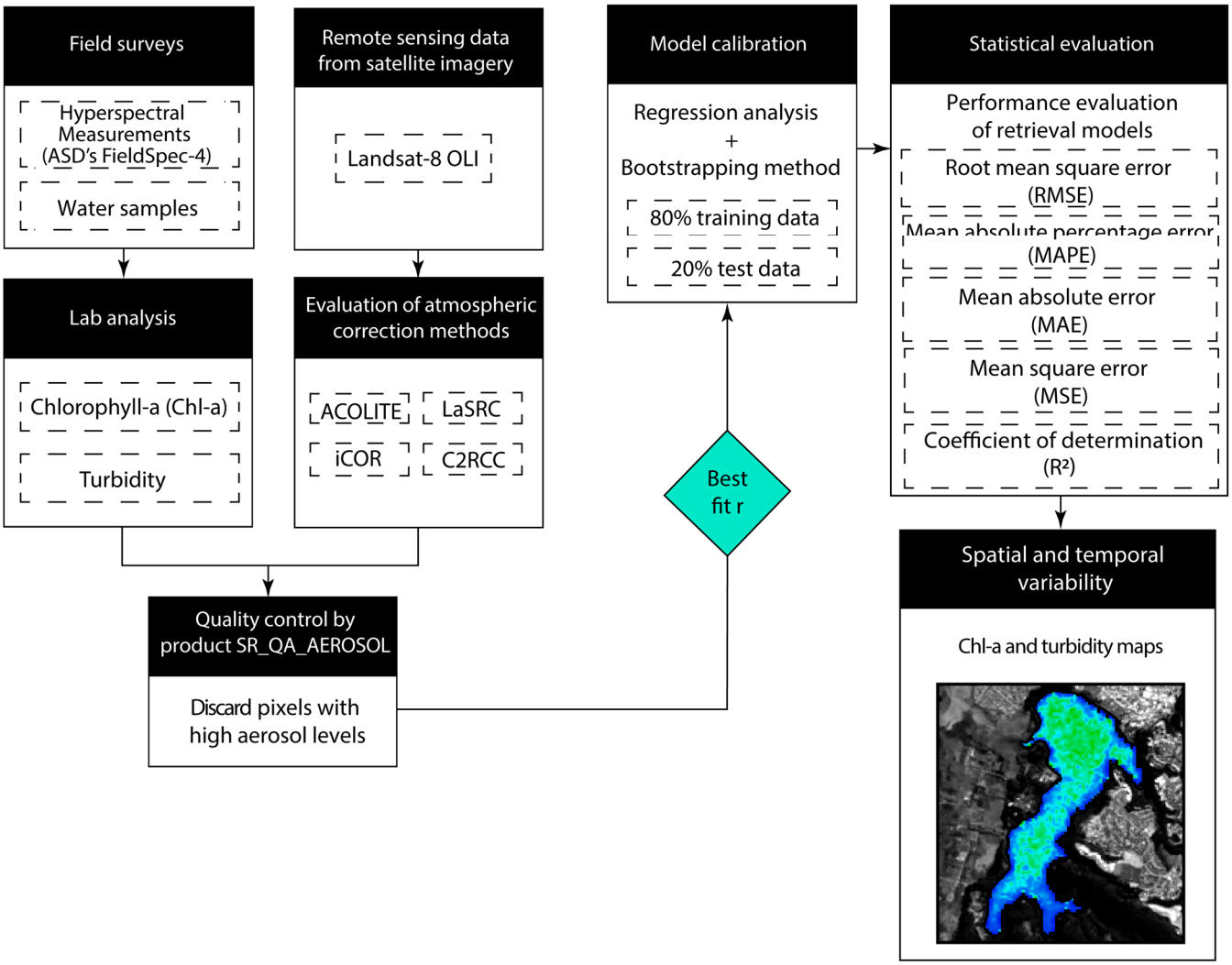

Figure 3. Workflow for the analysis of in situ and satellite imagery data.

The proposed methodology included the following main steps: (i) the in situ acquisition of spectral signatures, water sample collection, and OLI L-8 scene selection; (ii) the determination of Chl-a ($mg \cdot m^{-3}$) and turbidity (NTU) concentrations, and evaluation

of atmospheric correction models; (iii) atmospheric distortion pixel identification (high aerosol levels) to avoid introducing external error into the spectral retrieval model; (iv) the selection of spectral bands (with indices and reflectance band ratios) based on best-fit regressions with in situ values, ACOLITE and C2RCC being selected as the best atmospheric correction models to estimate Chl-a and turbidity values, respectively; (v) bootstrapping the statistical assessment to enhance the spectral retrieval model most suitable for each water quality parameter; furthermore, we used a set of five distinct statistical metrics to determine the precision and accuracy of the modeling process; and finally, (vi) the generation of spatiotemporal images for the water quality parameters at different dates and seasonal conditions.

2.6. Selection of Spectral Indices

Spectral indices are used to measure the distinctive characteristics of vegetation, water bodies and various land cover types [44]. Low-to-medium-resolution satellites have been widely used to develop eutrophic inland water classification algorithms and to retrieve the Chl-a concentration [45]. In terms of optics, Chl-a exhibits two points of highest reflectance, located in the green and near-infrared wavelength ranges at 550 nm and 700 nm, respectively [3]. A total of three spectral indices (Table 4) have been previously used to detect the presence of Chl-a in water by remote sensing.

The normalized difference vegetation index (NDVI) was calculated by the formula NDVI = (B5 − B4)/(B5 + B4), where "B5—NIR" represents the near-infrared spectral reflectance, predominantly influenced by plant canopy reflection, and "B4—Red" means the reflectance within the red part of the electromagnetic spectrum, where chlorophyll absorption reaches its maximum [46]. The green normalized difference vegetation index (GNDVI) [47] is based on the concept that an index designed to estimate chlorophyll content should remain constant regardless of pigments other than chlorophyll and should not be influenced by external factors, such as background or atmospheric conditions [48]. It is calculated by the formula GNDVI = (B5 − B3)/(B5 + B3), according to the band configuration of the OLI L-8 sensor. The green chlorophyll index (GCI) [49,50] is used to assess the chlorophyll content of leaves. An assessment of Chl-a content can be improved by including both near-infrared (NIR) and green wavelengths (GCI) [44], calculated by the following equation GCI = (B5/B3) − 1.

The turbidity parameter evaluation was based on previous studies [11,44,51,52]. These showed that reflectance values in the red and NIR bands had a strong correlation with suspended sediment concentration and turbidity levels. As a result, these spectral bands are considered as crucial indicators for assessing turbidity in water bodies [52]. Then, an empirical regression analysis technique was used to establish a relationship between field measurements and satellite data. For turbidity (NTU) estimation, different standard combinations for this parameter (Table 4) were applied, including NIR/red, NIR, blue/green, red + NIR, together with the normalized difference turbidity index (NDTI) [51].

Table 4. Main band and indices combinations used to estimate Chl-a and turbidity in Laguna Grande.

Parameter	Indices/Band Combinations	Formula	Reference
Chl-a	Normalized difference vegetation index (NDVI)	(B5 − B4)/(B5 + B4)	[46]
	Green normalized difference vegetation index (GNDVI)	(B5 − B3)/(B5 + B3)	[48]
	Green chlorophyll index (GCI)	(B5/B3) − 1	[50]
Turbidity	Near infrared/red	B5/B4	[53]
	Near-infrared	B5	[11]
	Blue/green	B2/B3	[44]
	Red + near-infrared	B4 + B5	[44]
	Normalized difference turbidity index (NDTI)	(B4 − B3)/(B4 + B3)	[51]
	Red	B4	[52]

2.7. Statistical Assessment

To assess the effectiveness of the selected bio-optical models, five statistical and error metrics were implemented, i.e., the mean absolute error (MAE; Equation (3)), the mean squared error (MSE; Equation (4)), the root-mean-square error (RMSE; Equation (5)), the mean absolute percent error (MAPE; Equation (6)), and the well-known coefficient of determination (R^2; Equation (7)). Additionally, to estimate the uncertainty in the correlation analysis, a bootstrapping methodology was applied in the assessment of Chl-a and turbidity obtained by spectral indices and in situ data. Bootstrapping involved creating multiple datasets by sampling with replacement from our original dataset, and then calculating the correlation in each of these sets. Thus, 1000 iterations of the bootstrap analysis were performed, using 80% of the dataset in each iteration to compute correlation and the remaining 20% for validation.

$$\mathrm{MAE} = \frac{\sum_{i=1}^{N} \left| X_i^{\mathrm{estimated}} - X_i^{\mathrm{measured}} \right|}{N} \quad (3)$$

$$\mathrm{MSE} = \frac{1}{n} \times \sum_{i=1}^{n} \left(X_i^{\mathrm{estimated}} - X_i^{\mathrm{measured}} \right)^2 \quad (4)$$

$$\mathrm{RMSE} = \sqrt{\frac{1}{n} \times \sum_{i=1}^{n} \left(X_i^{\mathrm{estimated}} - X_i^{\mathrm{measured}} \right)^2} \quad (5)$$

$$\mathrm{MAPE} = \frac{100}{n} \times \sum_{i=1}^{n} \left(\frac{X_i^{\mathrm{estimated}} - X_i^{\mathrm{measured}}}{X_i^{\mathrm{estimated}}} \right) \quad (6)$$

$$R^2 = 1 - \frac{SS_{\mathrm{res}}}{SS_{\mathrm{tot}}} \quad (7)$$

3. Results

3.1. Field Measurements of Water Parameters

In total, 85 water samples were collected under different seasonal conditions. For the first phase of the study, 40 measurements of Chl-a and turbidity were carried out to generate concentration maps by interpolating the obtained values. The purpose of that was to identify the areas of the lake with low, intermediate, and high concentration levels, as well as highlight areas with the largest variations in those values. This information allowed us to optimize subsequent field surveys, reducing the number of samples required to cover the entire lake to 20–25 stations. As nearby stations exhibited similar values, stations with the highest variations in Chl-a and turbidity were selected to build the spectral retrieval model. Thus, to improve the efficiency of data collection during the last two field trips, our work was focused on the stations and lake areas with the highest variability in Chl-a and turbidity values. In these field surveys, performed between 2022 and 2023, a maximum Chl-a value of 8.7 $mg{\cdot}m^{-3}$ was recorded during the near-fall season, while the lowest Chl-a with values of 2.2 $mg{\cdot}m^{-3}$ was observed during the summer season, in 2023. The mean Chl-a values recorded in each fieldwork were: 4.7 $mg{\cdot}m^{-3}$ in the spring season; 3.4 $mg{\cdot}m^{-3}$ in the summer season; and a value of 6.4 $mg{\cdot}m^{-3}$ during the season close to fall. According to Carlson's classification [5], Laguna Grande maintains a mesotrophic state, i.e., a moderate productivity was recorded for all of the evaluated seasons. Regarding turbidity values, a maximum of 20.2 NTU was also recorded in the near-fall season, while the lowest value of 0.6 NTU was observed during the summer season. The mean values for the field surveys were 2.4 NTU (spring season), 6.4 NTU (summer season), and 7.3 NTU (near the fall season). The average values did not exceed 5 NTU in the spring and summer seasons, so it could be considered a low turbidity value, typically associated with well-preserved clean waters. However, there was an increase in turbidity values near the fall season with values above 5 NTU, representing a moderate turbidity, which could be related to an increase in suspended sediment concentrations or biological activity.

3.2. Atmospheric Correction

3.2.1. Evaluation of Aerosol Levels at the Sampling Station Points

In situ spectral signatures of the water surface were used to compare the four atmospheric correction methods. The closest L-8 OLI image, acquired on 9 January 2023 (just three days apart), was used to collect the water spectral library. The implementation of the LaSRC SR_QA_AEROSOL product helped to identify suitable sampling stations for comparing in situ data with reflectance band combinations (Figure 4).

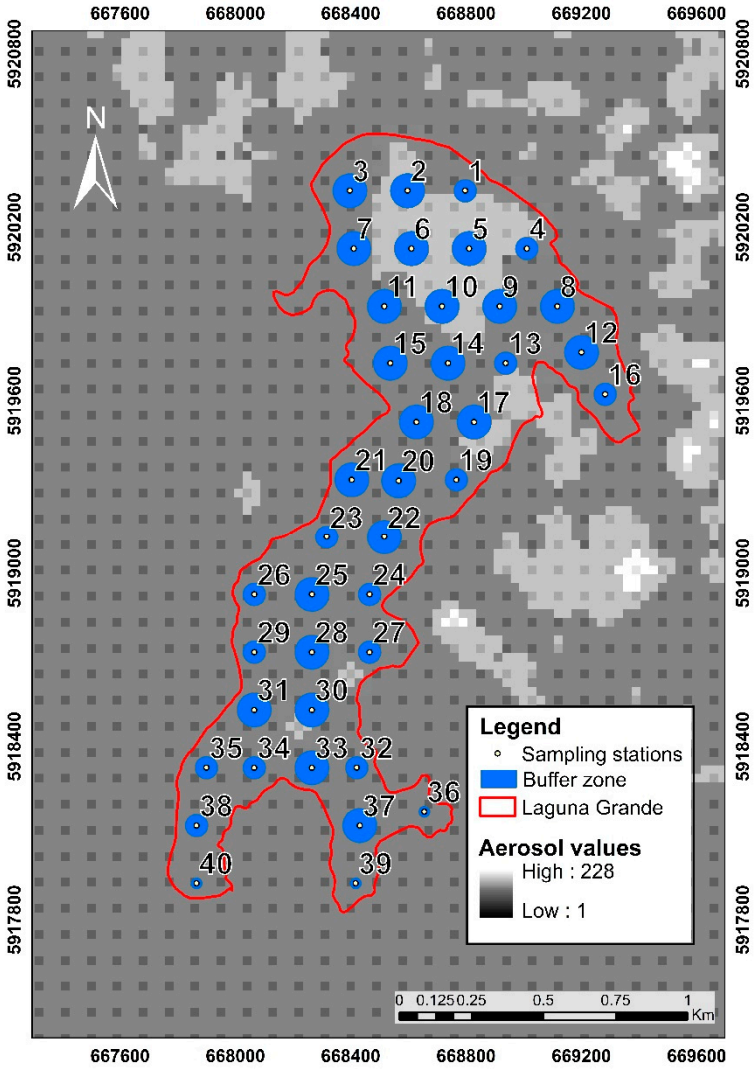

Figure 4. Chl-a and turbidity sampling stations were systematically located by covering a buffer of 60, 40, and 20 m over the LaSRC model quality image, which represents the aerosol levels in the scene (applying only a buffer of 40 and 20 m to those stations close to the lakeshore). Note that those stations located in pixels with high aerosol values were excluded from the correlation process.

Data processing began with the location of the station points on the map. To extract the reflectance values from the scene, buffer zones were calculated around each station with 60 m, 40 m, and 20 m buffer sizes to improve reflectance representativity. In the case of stations located near the shore, a coherent buffer size of 40 m and 20 m was applied to avoid lake shore interference. This adjustment was intended to mitigate spectral mixing between reflectance signals from water and soil materials, thus avoiding wrong model interpretations. The LaSRC SR_QA_AEROSOL product was used to select those pixels that were not affected by high aerosol values, ensuring better correlations between the in situ data and the results of the band combinations (Table 5).

Table 5. Adaptation of Landsat 8-9 SR_QA_AEROSOL values table.

Attribute	Pixel Value (DN)
Low-level aerosol	66, 68, 96, 100
Medium-level aerosol	130, 132, 160, 164
High-level aerosol	192, 194, 196, 224, 228

3.2.2. Evaluation of Atmospheric Correction Methods

The four atmospheric correction methods (ACOLITE, iCOR, LaSRC, and C2RCC) were evaluated taking station 15 as a "clean" reference (i.e., with no aerosol contamination) (Figure 5). L-8 OLI SWIR bands were excluded as the analysis was focused on the coastal, blue, green, red, and NIR bands, which are the most sensitive wavelengths for Chl-a and turbidity estimation.

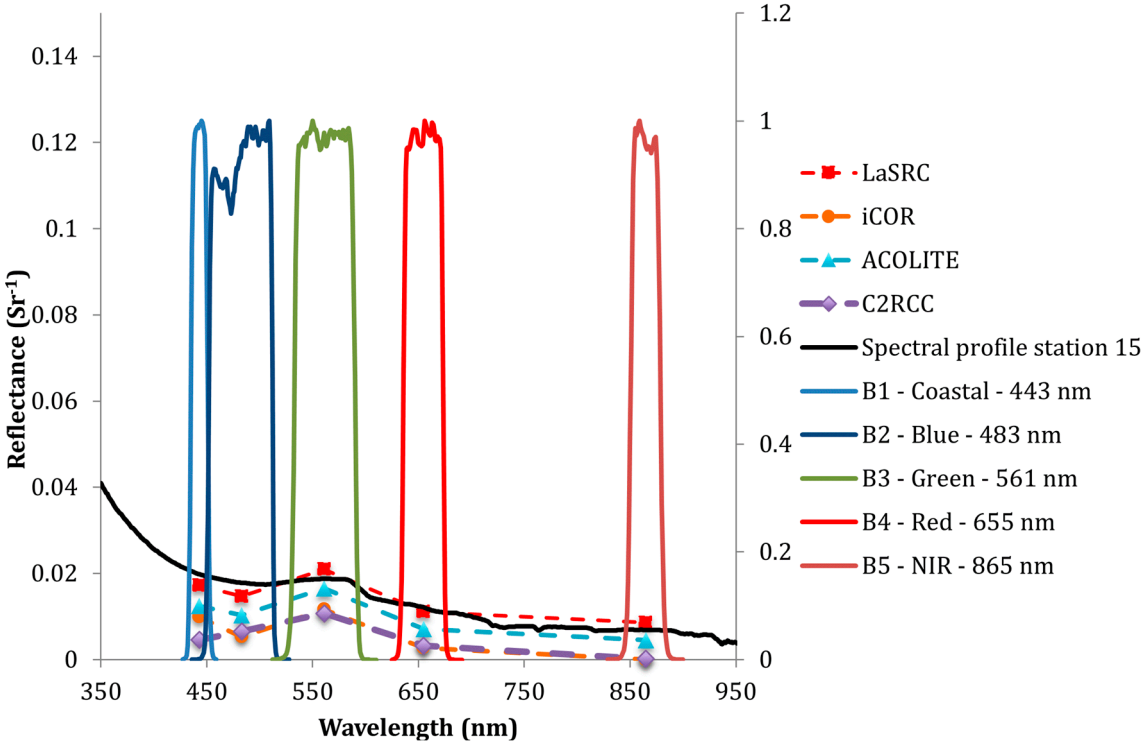

Figure 5. Comparison of atmospheric correction results and field radiometer data for the Laguna Grande lake. The black line depicts the measured water surface reflectance at station 15, which was collected by using the ASD Field-Spec 4 spectroradiometer.

Although collected data from seven stations were used for this comparison, for illustrative purposes only station 15 is shown in the results in Figure 5. The red segmented line, which corresponds to the LaSRC model's spectral signature, appears closer to the in situ measured reflectance (black line). However, in this model, an overestimation is highlighted in the B3 (green) and B5 (NIR) data, unlike other atmospheric correction models. This indicates that the LaSRC model did not consider the sun-glint effect on the water surface.

A comparison of satellite and field data showed that ACOLITE (cyan segmented line) yielded results more aligned with glint-free field measurements. Although the values in all bands were slightly lower than the in situ measured reflectance signature (black line), these maintained a similar shape, as well as that of the LaSRC method, but without showing saturation in B3 (green) and B5 (NIR). It is important to note that green and near-infrared bands are essential for Chl-a retrieval models. Chl-a absorbs light in the blue and red regions of the electromagnetic spectrum, while reflects light in the green and near-infrared regions [54]. This spectral property allows the estimation of Chl-a water concentration

by examining the reflectance ratio between the green and near-infrared bands. The iCOR (orange segmented line) and C2RCC (purple segmented line) models showed the worst fit compared to the in situ measured reflectance for all bands. In general, both models, iCOR and C2RCC, showed an underestimation in reflectance values. Therefore, ACOLITE was chosen as the optimal method to estimate Chl-a and turbidity.

3.3. Empirical Retrieval Models for Chl-a and Turbidity

3.3.1. Chl-a Estimation Analysis

Prior to analyzing the L-8 OLI reflectance, in situ Chl-a data were compared to the 15 spectral data values from the water surface, acquired with the ASD FieldSpec-4 spectroradiometer. The coefficient of determination (R^2) varied from 0.50 to 0.66 over the wavelength range from 350 to 1000 nm (Figure 6). R^2 values were greater than 0.6 in the red region from 650 nm, these wavelengths showing the best agreement. R^2 values showed a remarkable decrease around 925–950 nm (a region with wavelengths longer than the OLI NIR band), but those values quickly increased up to 0.66, even at wavelengths near 1000 nm.

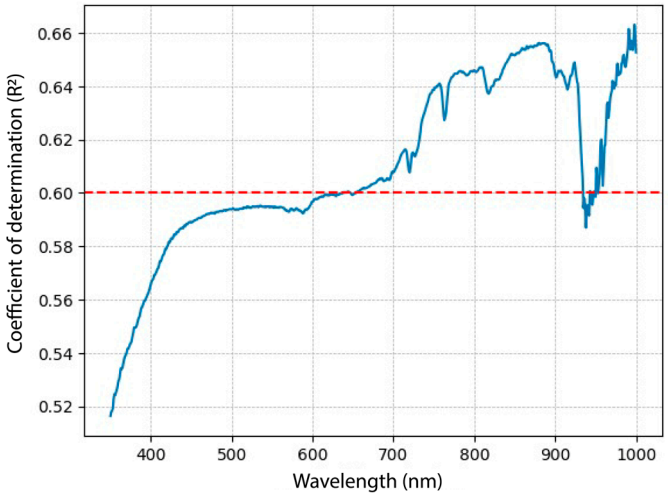

Figure 6. Correlation between water surface reflectance (spectral profiles) and Chl-a concentration determined from the field samples collected on 6 January 2023. Blue line: represents the Coefficient of Determination R^2 for all wavelengths between spectral profiles and in-situ data at the 15 stations. Red line: represents the best fit correlations (>0.60).

Chl-a has a unique absorption band that varies with its concentration, enabling the detection of specific spectral signatures through remote sensing. Results revealed that the absolute values at wavelengths of 655–880 nm and 990 nm exhibited the highest values of R^2. This suggests a stronger correlation between the Chl-a concentration and the reflectance at these specific wavelengths. R^2 values obtained for the relationship between the in situ Chl-a concentration and the reflectance values at 655 nm and 880 nm were 0.6 and 0.656, respectively (Figure 7). These coefficients indicate an important correlation in these spectral bands, aligning closely with the red and near-infrared (NIR) regions of the electromagnetic spectrum.

Pearson's coefficient values were used to assess the relationship between three vegetation indices and chlorophyll, i.e., NDVI, GNDVI, and GCI, and the Chl-a concentration values, using data from the green, red, and NIR regions. Notably, these indices (NDVI, GNDVI, and GCI) showed a statistically significant correlation ($p \leq 0.001$), with Pearson's coefficient values of -0.87 for NDVI and GNDVI, and -0.88 for GCI (Figure 8). Hence, GCI was selected as the best option to build the retrieval model. The sensitivity of the Chl-a concentration to multiband reflectance combinations is clearly demonstrated in Figure 8, highlighting its higher responsivity compared to a single-band reflectance.

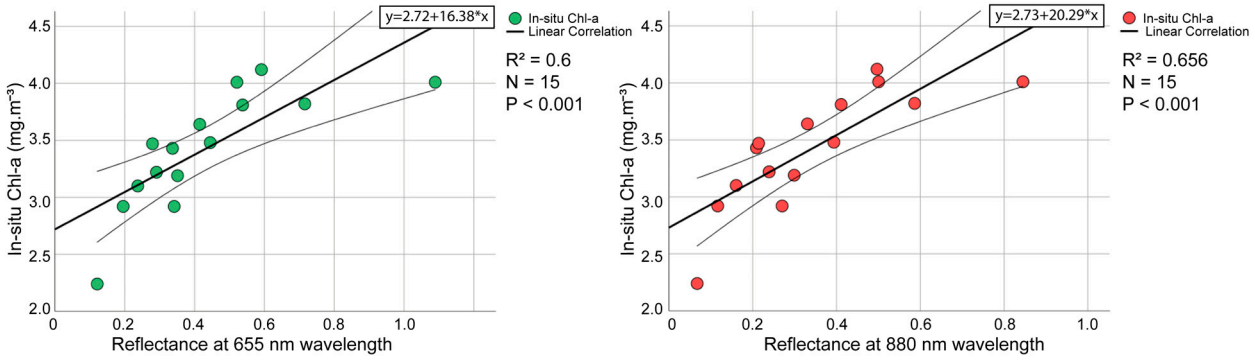

Figure 7. Relationship between Chl-a concentration and reflectance at wavelengths of 655 nm and 880 nm.

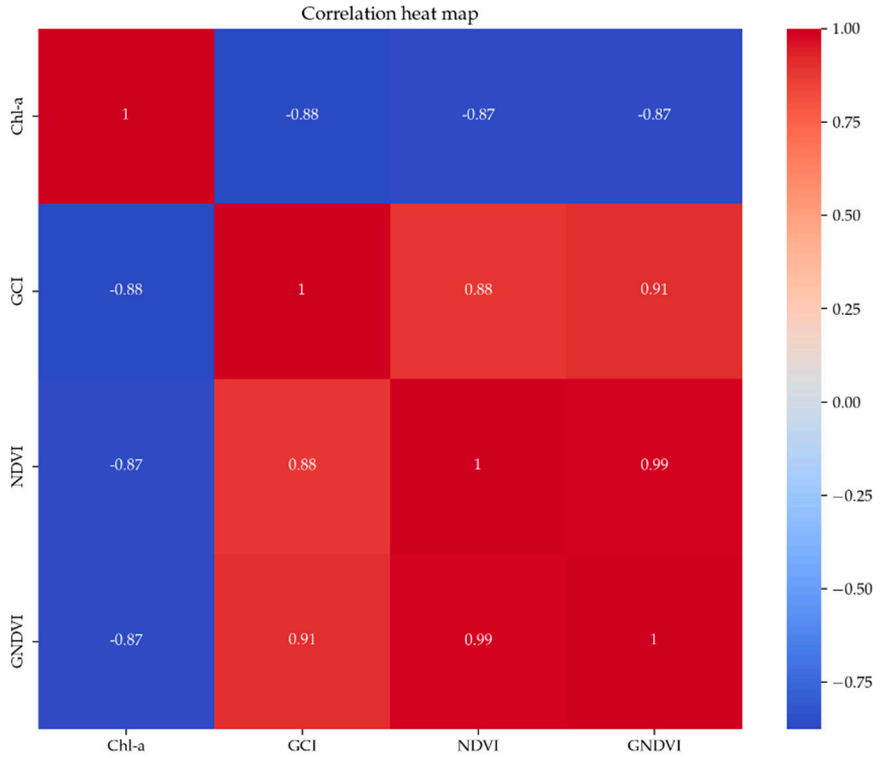

Figure 8. Heat map used to evaluate different spectral indices (GCI, NDVI and GNDVI) with in situ Chl-a data (mg·m^{-3}), using reflectance values from ACOLITE.

3.3.2. Turbidity Estimation Analysis

The turbidity values' estimation using satellite imagery was based on spectral indices and combinations of bands related to suspended material in the water. Several spectral indices and band combinations were evaluated: NIR, red, NIR/red, red + NIR, blue/green, and NDTI to determinate the best fit with turbidity values (Figure 9). The obtained correlation values were, from low to high: NIR (Pearson's coefficient = 0.098); NIR/red (Pearson's coefficient = −0.34); NDTI (Pearson's coefficient = 0.62); blue/green (Pearson's coefficient = −0.87); red (Pearson's coefficient = 0.87); and red + NIR (Pearson's coefficient = 0.88). The spectral indices with the best performance were blue/green, red, and notably, red + NIR, which showed statistically significant correlation ($p \leq 0.001$), with a Pearson's coefficient value of 0.88.

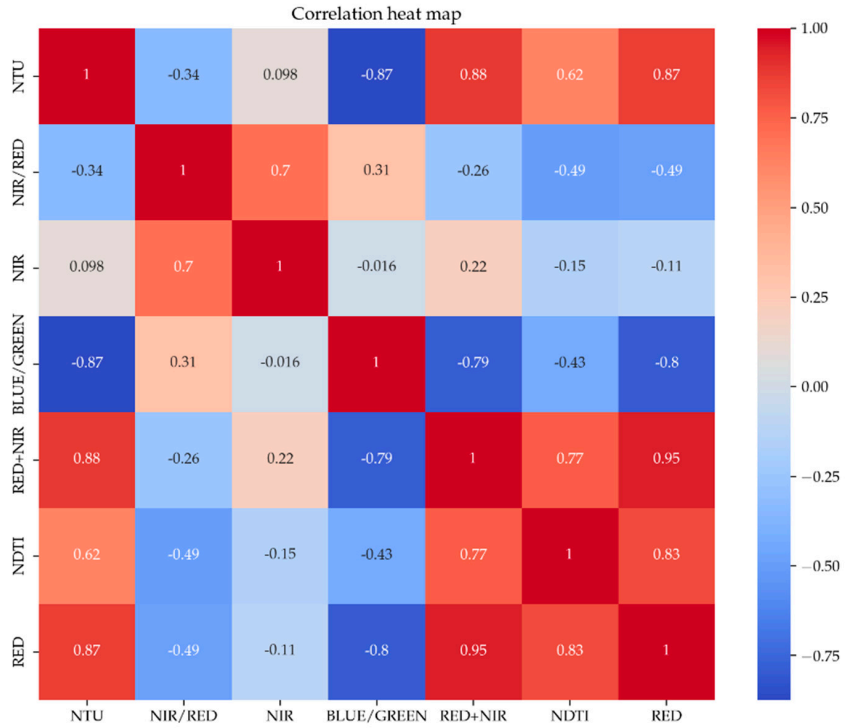

Figure 9. Heat map used to evaluate different band combinations (red, NDTI, red + NIR, blue/green, NIR, NIR/red, and NDTI) with in situ turbidity data (NTU) using ACOLITE reflectance.

3.4. Statistical Evaluation and Model Robustness

3.4.1. Statistical Evaluation and Robustness of the Chl-a Estimation Model

To assess the reliability of the correlation analysis between the Chl-a concentration and the GCI (best fit R^2), a bootstrapping technique was applied. Through 1000 iterations, the distribution of function parameters was obtained to optimize its selection between the mean and the median (Figure 10). Consequently, Equation (8) represents the final Chl-a retrieval model.

$$Chla = 1.97 \times e^{(-1.46 \times GCI)} \quad (8)$$

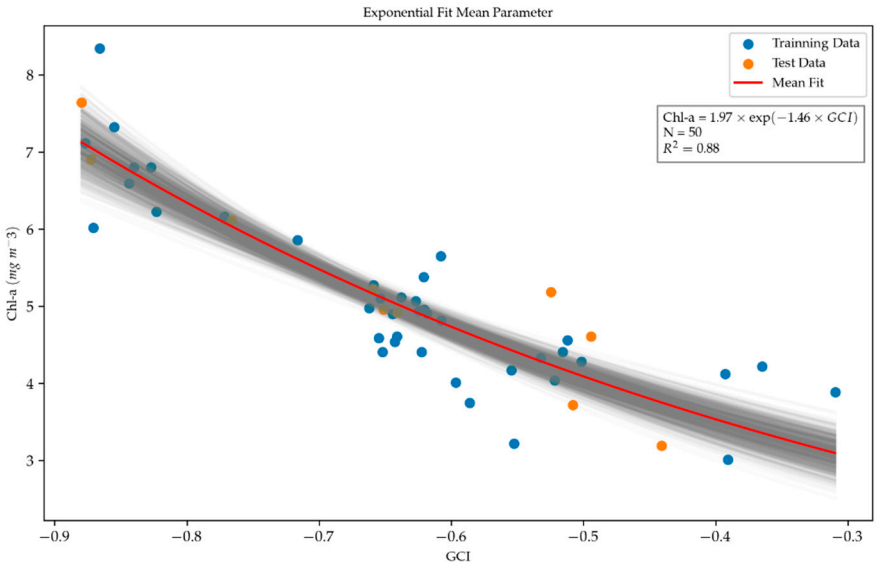

Figure 10. Calibration curve between the in situ Chl-a data and the GCI with the application of the bootstrapping technique, using the mean fit in the parameters with 1000 iterations, taking 80% of the dataset in each iteration to compute the correlation and the remaining 20% for validation.

Statistical and correlation metrics yielded robust results with R^2 = 0.88, MAE = 0.35, MSE = 0.20, RMSE = 0.45, and MAPE = 7.56%, ensuring the stability of the observed relationship (Figure 11). This bootstrapping approach helped to provide a robust and reliable estimation of the relationship between the variables.

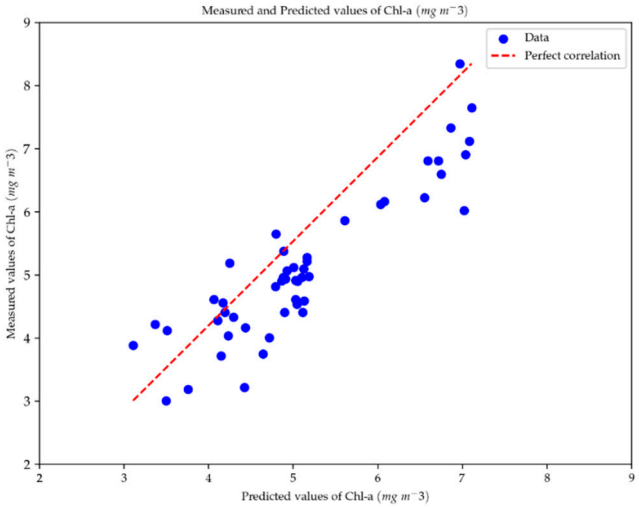

Figure 11. Comparison of Chl-a measured versus Chl-a estimated from Landsat-8 OLI images using the GCI algorithm (Equation (8)) with ACOLITE data (corrected reflectance).

To evaluate trends in estimation errors, we examined the model residuals using scatter plots against the in situ collection data. No discernible pattern emerged, indicating the absence of systematic trends in residual variations associated with changes in Chl-a concentration, the errors being randomly distributed (Figure 12). Residuals were uniformly scattered around zero, with all residual errors approximately within the range from −1 to 1.

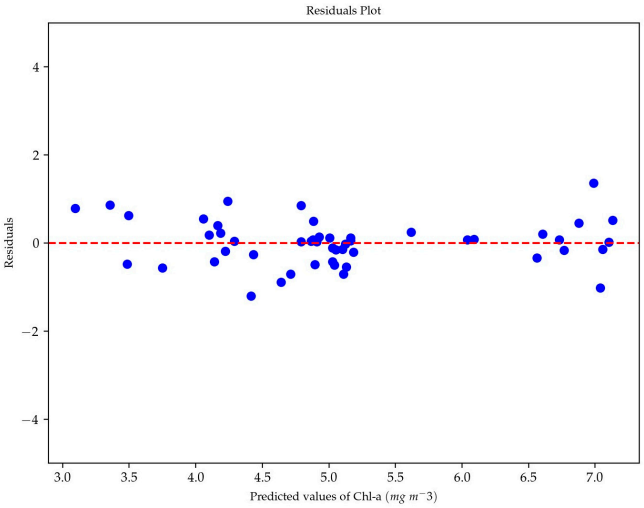

Figure 12. Chl-a residual values versus Chl-a predicted values (mg·m^{-3}), showing a low dispersion in the values over the whole Chl-a range, from 3 to 8 mg·m^{-3}.

3.4.2. Statistical Evaluation and Robustness of the Turbidity Estimation Model

As in the Chl-a estimation model, the bootstrapping method was performed using 1000 iterations to optimize the selection of function parameters between mean and median (Figure 13). As a result, Equation (9) is the final turbidity retrieval model.

$$Turbidity = 0.51 \times e^{(130.75 \times (Red + NIR))} \quad (9)$$

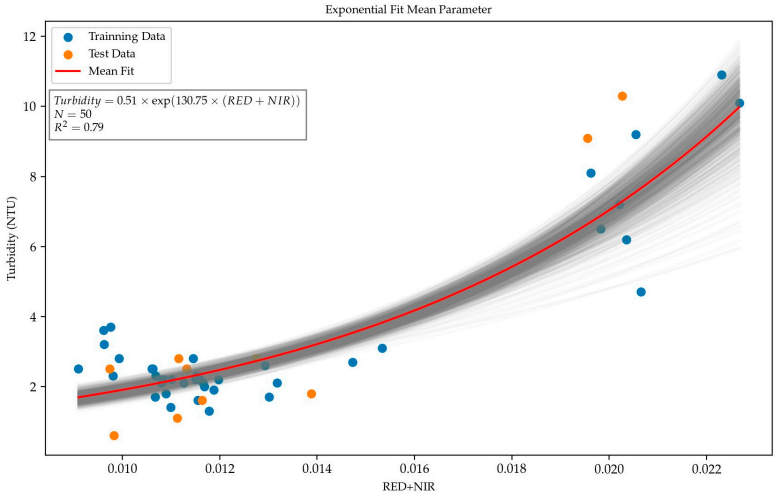

Figure 13. Calibration curve between the in situ turbidity (NTU) data and the red + NIR index with the application of the bootstrapping technique using the mean fit in the parameters with 1000 iterations, using 80% of the dataset in each iteration to compute the correlation and the remaining 20% for validation.

Statistical and correlation metrics also yielded intermediate results with R^2 = 0.79, MAE = 1.15, MSE = 2.11, RMSE = 1.45, and MAPE = 54.89% (Figure 14). The latest MAPE results were unsatisfactory as the error exceeded 10–20%. This suggests that the correlation between the red + NIR index and in situ turbidity data is not robust enough to be considered as a reliable estimation model.

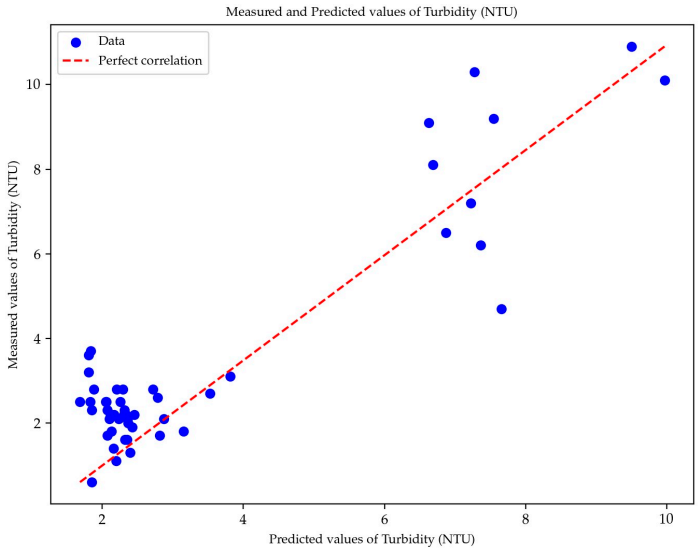

Figure 14. Comparison of turbidity measured versus turbidity estimated from Landsat-8 OLI images using the red + NIR algorithm (Equation (9)) with ACOLITE data (corrected reflectance).

Figure 15 shows the data clustering, with one cluster with very low values (<4 NTU) and another more dispersed cluster with slightly higher values (>7 NTU) from 7 to 10 NTU, suggesting a seasonal behavior in the data.

It is important to note that the turbidity levels in this lake are particularly lower than those in highly eutrophic lakes [55]. These low turbidity values may result in a relatively weak spectral relationship with reflectance bands.

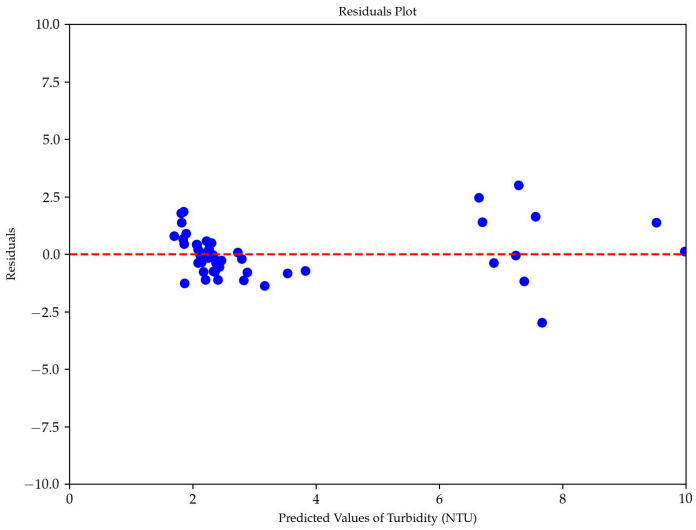

Figure 15. The residuals of in situ turbidity observations compared to predicted turbidity values (NTU) are represented by blue dots. Note that the data are not uniformly dispersed around zero, with all residual errors approximately within the range from −3.5 to 3.5 NTU.

3.5. Spatial and Temporal Variability

Statistical results showed a strong relationship (R^2 = 0.88) for the Chl-a retrieval model using the CGI, but the turbidity retrieval model did not accurately reproduce the in situ data. As a result, the time series analysis was focused on the Chl-a distribution variability across the lake (Figure 16).

The data for the Laguna Grande system consistently fell within the mesotrophic classification, with Chl-a concentration levels ranging from 3 to 10 mg·m^{-3} (Figure 17). These values implied a moderate level of biological productivity, which remained stable across the evaluated seasons and periods.

A detailed analysis comparing the 2014 and 2022 data (Figures 16 and 17) revealed fluctuating Chl-a mean values. Considering the year 2022, Chl-a values for the northern zone (Figure 17a, blue line) varied from 6.2 mg·m^{-3} in winter, dropping to 5.1 mg·m^{-3} in spring, increasing to 5.4 mg·m^{-3} in summer, and showing a peak at 7.1 mg·m^{-3} in fall. This pattern was consistent in both northern (Figure 17a, blue line) and southern zones of the lake. However, in the southern zone (Figure 17b, blue line), mean values were consistently lower for each season: 5.5 mg·m^{-3}, 4.6 mg·m^{-3}, 5.2 mg·m^{-3}, and 6.2 mg·m^{-3}, respectively.

A further check of the Chl-a dynamics for 2014 revealed a different pattern. In the northern zone (Figure 17a, red line), Chl-a values ranged from 7.4 mg·m^{-3} in winter, decreasing to 6.0 mg·m^{-3} in spring, reaching a peak of 6.7 mg·m^{-3} in summer, and then decreasing down to 6.2 mg·m^{-3} in the fall season. Meanwhile, the southern zone exhibited a similar trend, albeit with consistently lower mean values. The concentrations oscillated between 5.0 mg·m^{-3} and 6.2 mg·m^{-3} (Figure 17b, red line). This comparative analysis provided valuable insights into the seasonal Chl-a dynamics in both northern and southern zones, shedding light on how these patterns evolved over time.

The obtained Chl-a values consistently exhibit higher levels in the northern zone compared to the southern zone, regardless of the year (2022 versus 2014; Figure 17). This disparity might be attributed to a more pronounced anthropic impact in the northern zone, characterized by rapid urban sprawl over recent years, while the southern zone, which is bordered by dense vegetation, remained relatively unchanged. Recent regulations implemented by local authorities restricting activities that promote lake pollution have further reinforced this trend. Notably, the Chl-a values for 2022 were lower than those observed in 2014, aligning with government restrictions on lake access, such as the use of fuel-powered boats and new construction around the lake shore.

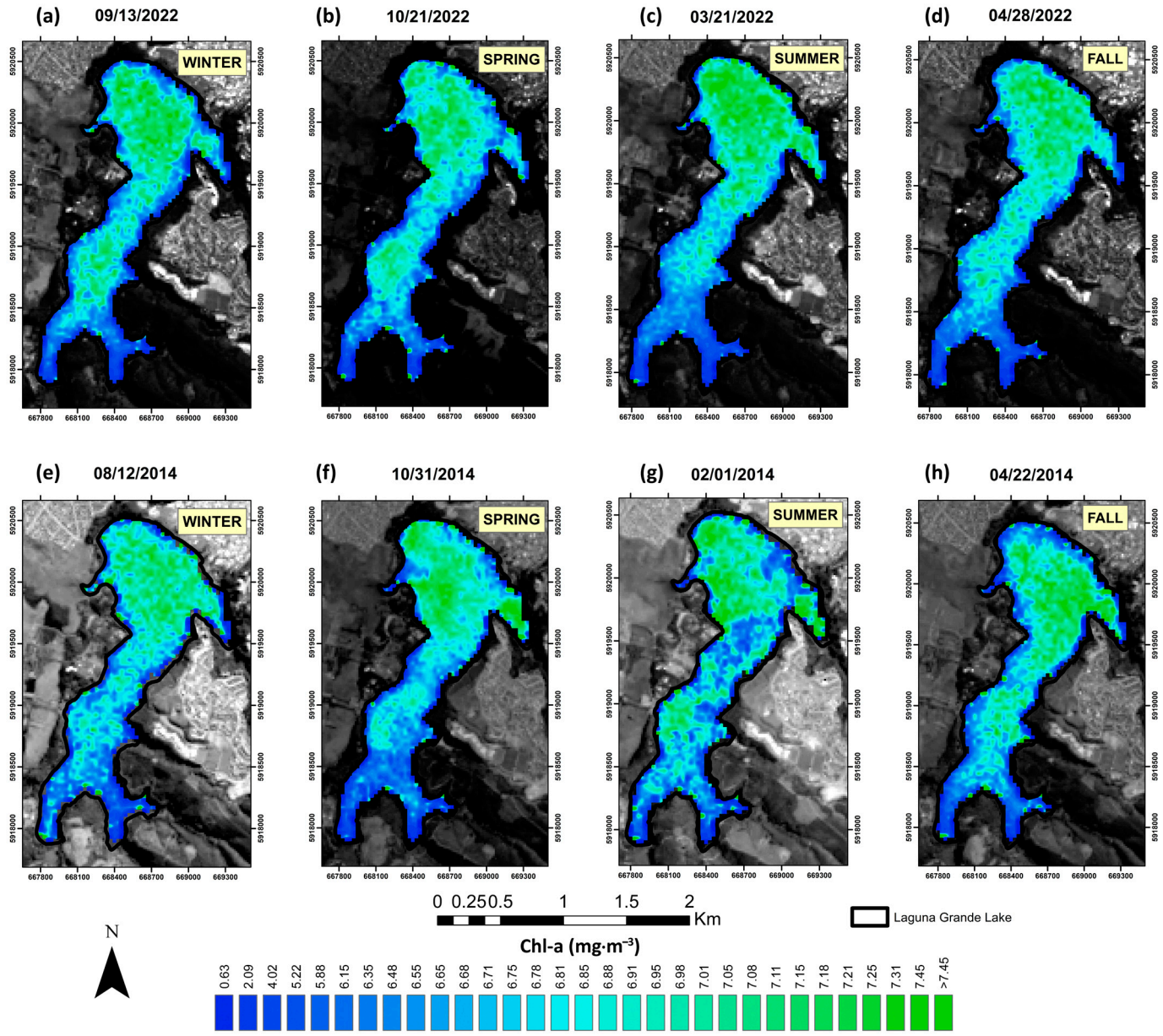

Figure 16. Chl-a distribution maps for Laguna Grande showing the variation in concentration values for winter, spring, summer, and fall seasons in 2022 (**a**–**d**) and 2014 (**e**–**h**).

Upon closer examination, when comparing the summer and fall data for 2014 (Figure 17, red line), an anticipated trend was revealed: a decrease in Chl-a values from 6.2 mg·m^{-3} to 5.6 mg·m^{-3}. This behavior is aligned with the expected decline in the temperature records between these two seasons. However, a contrasting pattern emerged when the data for 2022 were analyzed (Figure 17, blue line), where Chl-a values recorded for the fall surpassed those for the summer season. This unexpected behavior can be attributed to the fact that recent autumnal temperatures resemble historical summer temperatures, possibly driven by regional climate variability. These findings highlight the OLI sensor potential in forecasting algal bloom distribution and trophic state in the lake.

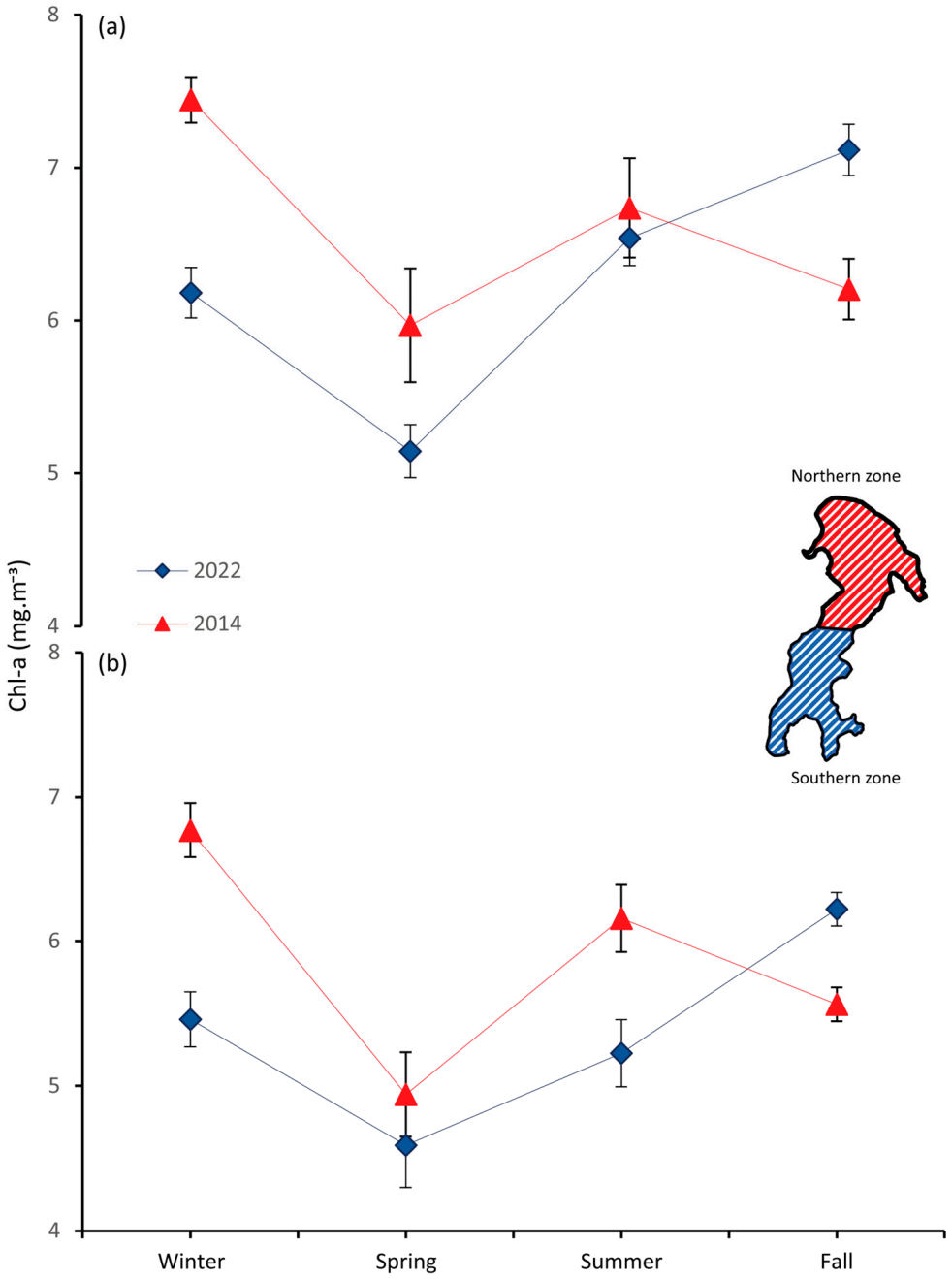

Figure 17. Spider diagram illustrating Chl-a variability across seasons in the northern (**a**) and southern (**b**) zones. Mean values for 2022 (blue line) and 2014 (red line) are depicted, highlighting the region of interest within each lake section.

4. Discussion

The main findings in the development of spectral retrieval models for water quality parameters in Laguna Grande can be summarized into three key issues:

(i) Implementation of atmospheric correction methods

In this study, the first water quality analysis in Laguna Grande was performed by applying an innovative methodology, which involved the collection of in situ data (water quality parameters), combined with spectral signatures at the water surface using ground-based radiometers. These measurements were then integrated to calibrate and validate the reflectance signal of the multispectral satellite images (OLI sensor) using different atmospheric correction methods. ACOLITE provided results that closely matched with

glint-free field measurements. Although the values in all bands were slightly lower than the actual reflectance signatures (surface water spectral profile), they retained a similar shape. When comparing the in situ Chl-a and turbidity data to the reflectance signals corrected by the different atmospheric methods, ACOLITE showed the highest coefficients of determination, reaching R^2 values of 0.88 and 0.79 for Chl-a and turbidity, respectively. These results are in line with a recent study conducted by Rodríguez-López et al. [9], in which ACOLITE was used as an atmospheric distortion mitigation method on L-8 OLI scenes to estimate Chl-a concentrations in the Llanquihue Lake (Southern Chile). Other water quality research studies have found that ACOLITE effectively corrects for atmospheric distortions in water bodies, especially in the development of Chl-a estimation models from L-8 satellite OLI scenes (e.g., [56–58]). Additionally, this study confirms the essential role of a rigorous atmospheric correction to mitigate errors from aerosols and the sun-glint effect during the construction of spectral inversion models from satellite imagery. As discussed in Yépez et al. [11], the utilization of the USGS LaSRC SR_QA_AEROSOL product aids in filtering out pixels affected by atmospheric distortions, improving the relationship between in situ data and image reflectance, even in cases of temporal disparities between data collection and scene acquisition.

(ii) Development of an empirical retrieval model

The green chlorophyll index (GCI) was selected as the optimal choice for constructing the Chl-a retrieval model in Laguna Grande, despite being a spectral index used in terrestrial applications [49]. Results showed a remarkable sensitivity for Chl-a concentration to various multiband reflectance combinations, underlining the high responsiveness of this index. Similar results were observed in other water quality studies, where spectral indices such as the NDVI and GNDVI were used (e.g., [59–61]). The CGI showed the highest relationship with an R^2 value of 0.88, making it the best choice for the Chl-a retrieval model in the study lake. The robustness of the model was assessed by the bootstrapping method, confirming its statistical significance. Results were also in line with previous studies that showed a strong agreement (R^2 = 0.73) with the B5 (near-infrared)/B3 (green) spectral ratio index derived from the OLI sensor and in situ Chl-a levels [53].

The analysis of turbidity parameters showed that the red + NIR spectral index achieved the highest R^2 value, reaching 0.79. However, a high MAPE of 54.89% showed model weaknesses, indicating a lack of robustness. The data also showed a seasonal dynamic, which highlights the importance of collecting winter data (water samples) to overcome the limitation of this retrieval model. Thus, to account for the seasonality factor comprehensively, it is advisable to incorporate data from several seasons into the model training.

(iii) Assessment of the spatial–temporal variability

Finally, results clearly showed a spatial pattern with higher Chl-a values in the northern zone compared to the southern zone. These results are in agreement with those of Pedrero-Guarda et al. [25], who identified spatial dynamics of temperature in Laguna Grande, possibly attributed to a heat island effect. This effect causes temperature differences, with higher temperatures near urban areas (northern part) and lower temperatures in vegetated regions. Since Chl-a levels are affected by factors such as nutrients, phosphorus, pH, water flow, and temperature, it is plausible that this temperature gradient contributed to generate the higher Chl-a levels in the northern part of the lake.

5. Conclusions

This study marks the first step towards the development of a web platform that will provide access to water quality data derived from satellite signals, such as Landsat-8 OLI, for the main lakes of Chile. A positive result of this study arose when evaluating Chl-a values estimated from OLI images between 2014 and 2022. In general, a decrease in Chl-a concentrations was observed throughout the Laguna Grande lake, which can be attributed to recent local regulations aimed at reducing activities that caused lake pollution. However, it will be necessary to evaluate a time series at a monthly scale to determine whether this

decline is maintained. For this purpose, further analysis will be carried out at Laguna Grande. This task seeks to improve spectral estimation models by integrating airborne hyperspectral technology using NEO's HySpex VNIR-1800 cameras. In addition, in situ data will be collected covering various water quality parameters in different seasons. The results of this study are expected to promote the use of Earth observation data in inland water quality monitoring, ultimately supporting sustainable water resource management.

Author Contributions: Conceptualization, S.Y., L.R.-L. and G.V.; methodology, S.Y., L.R.-L. and G.V.; software, D.T., S.Y., R.S.-P., H.C., N.F., M.P. and A.C.; validation, J.C., X.P., F.F. and L.R.-L.; formal analysis, S.Y. and D.T.; investigation, S.Y., D.T. and G.V.; resources, S.Y.; data curation, D.T.; writing—original draft preparation, S.Y., G.V. and D.T.; writing—review and editing, S.Y., D.T., G.V., H.C., A.C., N.F., F.F., L.B., J.C., X.P. and L.R.-L.; visualization, D.T., S.Y. and R.S.-P.; supervision, S.Y., G.V., F.F. and L.B.; project administration, S.Y.; funding acquisition, S.Y. and G.V. All authors have read and agreed to the published version of the manuscript.

Funding: This research was funded by the Chilean government through ANID's Fondecyt Regular Project no. 1221091.

Data Availability Statement: The datasets produced and analyzed in the course of this study can be obtained upon reasonable request from the corresponding author. The data are not publicly available due to privacy restrictions.

Acknowledgments: S.Y. and G.V. are grateful for ANID's support through the Fondecyt Regular project 1221091. We are also grateful for the support provided by the staff of the EULA center from the University of Concepcion in data collection at the lake and for the laboratory analysis. S.Y. appreciates the assistance from Forestal ARAUCO S.A.'s Planning and Continuous Improvement Management team for their support in supplying equipment and guidance during field activities. G.V. has been supported through the grant EUR TESS no. ANR-18-EURE-0018 in the framework of the Programme des Investissements d'Avenir. D.T. extends appreciation to Professor César Rubén Fernández De Villarán at the University of Huelva for his support during a stay in Spain and acknowledges the AUIP for facilitating this mobility experience. X.P. is the recipient of an ICREA Academia Excellence in Research Grant (2023–2027). Landsat Surface Reflectance products were downloaded from the U.S. Geological Survey. We are grateful to the reviewers for comments that greatly improved this article.

Conflicts of Interest: Martin Pincheira was employed by the company Forestal ARAUCO S.A. The remaining authors declare that the research was conducted in the absence of any commercial or financial relationships that could be construed as a potential conflict of interest.

References

1. Millennium Ecosystem Assessment. *Ecosystems and Human Well-Being*; Island Press: Washington, DC, USA, 2005.
2. Cooke, G.D.; Welch, E.B.; Peterson, S.; Nichols, S.A. *Restoration and Management of Lakes and Reservoirs*; CRC Press: Boca Raton, FL, USA, 2016.
3. Abdelal, Q.; Assaf, M.N.; Al-Rawabdeh, A.; Arabasi, S.; Rawashdeh, N.A. Assessment of Sentinel-2 and Landsat-8 OLI for small-scale inland water quality modeling and monitoring based on handheld hyperspectral ground truthing. *J. Sens.* **2022**, *2022*, 4643924. [CrossRef]
4. Van Rees, C.B.; Waylen, K.A.; Schmidt-Kloiber, A.; Thackeray, S.J.; Kalinkat, G.; Martens, K.; Domisch, S.; Lillebø, A.I.; Hermoso, V.; Grossart, H.P. Safeguarding freshwater life beyond 2020: Recommendations for the new global biodiversity framework from the European experience. *Conserv. Lett.* **2021**, *14*, e12771. [CrossRef]
5. Carlson, R.E. A trophic state index for lakes 1. *Limnol. Oceanogr.* **1977**, *22*, 361–369. [CrossRef]
6. Lei, F.; Yu, Y.; Zhang, D.; Feng, L.; Guo, J.; Zhang, Y.; Fang, F. Water remote sensing eutrophication inversion algorithm based on multilayer convolutional neural network. *J. Intell. Fuzzy Syst.* **2020**, *39*, 5319–5327. [CrossRef]
7. Huang, Z.; Wu, X.; Wang, H.; Hwang, C.; He, X. Monitoring Inland Water Quantity Variations: A Comprehensive Analysis of Multi-Source Satellite Observation Technology Applications. *Remote Sens.* **2023**, *15*, 3945. [CrossRef]
8. Peterson, K.T.; Sagan, V.; Sloan, J.J. Deep learning-based water quality estimation and anomaly detection using Landsat-8/Sentinel-2 virtual constellation and cloud computing. *GIScience Remote Sens.* **2020**, *57*, 510–525. [CrossRef]
9. Rodríguez-López, L.; Usta, D.B.; Duran-Llacer, I.; Alvarez, L.B.; Yépez, S.; Bourrel, L.; Frappart, F.; Urrutia, R. Estimation of Water Quality Parameters through a Combination of Deep Learning and Remote Sensing Techniques in a Lake in Southern Chile. *Remote Sens.* **2023**, *15*, 4157. [CrossRef]

10. Sòria-Perpinyà, X.; Vicente, E.; Urrego, P.; Pereira-Sandoval, M.; Ruíz-Verdú, A.; Delegido, J.; Soria, J.M.; Moreno, J. Remote sensing of cyanobacterial blooms in a hypertrophic lagoon (Albufera of València, Eastern Iberian Peninsula) using multitemporal Sentinel-2 images. *Sci. Total Environ.* **2020**, *698*, 134305. [CrossRef]
11. Yepez, S.; Laraque, A.; Martinez, J.-M.; De Sa, J.; Carrera, J.M.; Castellanos, B.; Gallay, M.; Lopez, J.L. Retrieval of suspended sediment concentrations using Landsat-8 OLI satellite images in the Orinoco River (Venezuela). *Comptes Rendus Geosci.* **2018**, *350*, 20–30. [CrossRef]
12. Steissberg, T.; Schladow, G.; Hook, S. *Monitoring Past, Present, and Future Water Quality Using Remote Sensing*; Tahoe Environmental Research Center and Jet Propulsion Laboratory (NASA): Pasadena, CA, USA, 2010; Volume 108.
13. Niroumand-Jadidi, M.; Bovolo, F.; Bresciani, M.; Gege, P.; Giardino, C. Water quality retrieval from landsat-9 (OLI-2) imagery and comparison to sentinel-2. *Remote Sens.* **2022**, *14*, 4596. [CrossRef]
14. Abbas, M.; Rasib, A.; Ahmad, B.; Musa, T.; Abbas, T.; Dutsenwai, H. Landsat data to estimate a model of water quality parameters in Tigris and Euphrates Rivers—Iraq. *Int. J. Adv. Appl. Sci.* **2019**, *6*, 50–58. [CrossRef]
15. Normandin, C.; Lubac, B.; Sottolichio, A.; Frappart, F.; Ygorra, B.; Marieu, V. Analysis of suspended sediment variability in a large highly turbid estuary using a 5-year-long remotely sensed data archive at high resolution. *J. Geophys. Res. Ocean.* **2019**, *124*, 7661–7682. [CrossRef]
16. Olmanson, L.G.; Brezonik, P.L.; Bauer, M.E. Remote sensing for regional lake water quality assessment: Capabilities and limitations of current and upcoming satellite systems. In *Advances in Watershed Science and Assessment*; Springer International Publishing: Cham, Switzerland, 2015; pp. 111–140.
17. Schaeffer, B.A.; Schaeffer, K.G.; Keith, D.; Lunetta, R.S.; Conmy, R.; Gould, R.W. Barriers to adopting satellite remote sensing for water quality management. *Int. J. Remote Sens.* **2013**, *34*, 7534–7544. [CrossRef]
18. Li, W.; Zhou, Y.; Yang, F.; Liu, H.; Yang, X.; Fu, C.; He, B. Using C2X to Explore the Uncertainty of In Situ Chlorophyll-a and Improve the Accuracy of Inversion Models. *Sustainability* **2023**, *15*, 9516. [CrossRef]
19. Ha, N.T.T.; Thao, N.T.P.; Koike, K.; Nhuan, M.T. Selecting the best band ratio to estimate chlorophyll-a concentration in a tropical freshwater lake using sentinel 2A images from a case study of Lake Ba Be (Northern Vietnam). *ISPRS Int. J. Geo-Inf.* **2017**, *6*, 290. [CrossRef]
20. Parra, O.O. La eutroficación de la Laguna Grande de San Pedro, Concepción, Chile: Un caso de estudio. *Ambiente Desarro.* **1989**, *V*, 117–136.
21. Garg, V.; Kumar, A.S.; Aggarwal, S.; Kumar, V.; Dhote, P.R.; Thakur, P.K.; Nikam, B.R.; Sambare, R.S.; Siddiqui, A.; Muduli, P.R. Spectral similarity approach for mapping turbidity of an inland waterbody. *J. Hydrol.* **2017**, *550*, 527–537. [CrossRef]
22. Lillo-Saavedra, M.F.; Gonzalo, C. Aplicación de la Metodología de Fusión de Imágenes Multidirección-Multiresolución (MDMR) a la Estimación de la Turbidez en Lagos. *Inf. Tecnológica* **2008**, *19*, 137–146. [CrossRef]
23. Quintana-Sotomayor, C.; Lillo-Saavedra, M.; Gonzalo-Martín, C.; Barrera-Berrocal, J.A. Metodología para estimación de la turbidez de un lago mediante la clasificación orientada a objetos de imágenes multiespectrales. *Tecnol. Cienc. Agua* **2012**, *3*, 143–150.
24. Rojas Jordán, A. *Evaluación de los Efectos del Cambio de Uso de Suelo Sobre las Tasas de Sedimentación en Laguna Grande de San Pedro de la Paz (Chile) Durante los Últimos 30 Años*; Universidad de Concepción: Concepción, Chile, 2018.
25. Pedreros-Guarda, M.; Abarca-del-Río, R.; Escalona, K.; García, I.; Parra, Ó. A Google Earth Engine application to retrieve long-term surface temperature for small lakes. Case: San Pedro lagoons, Chile. *Remote Sens.* **2021**, *13*, 4544. [CrossRef]
26. Cruces, F.; Urrutia, R.; Araneda, A.; Torres, L.; Cisternas, M.; Vyverman, W. Evolución trófica de Laguna Grande de San Pedro (VIII Región, Chile) durante el último siglo, mediante el análisis de registros sedimentarios. *Rev. Chil. Hist. Nat.* **2001**, *74*, 407–418. [CrossRef]
27. Urrutia, R. Estudio del estado trófico de los cuerpos de agua existentes en San Pedro de la Paz. In Proceedings of the Seminario EULA, Concepción, Chile, 28 October 2021.
28. Arar, E.J.; Collins, G.B. *Method 445.0: In Vitro Determination of Chlorophyll a and Pheophytin a in Marine and Freshwater Algae by Fluorescence*; United States Environmental Protection Agency, Office of Research and Development, National Exposure Research Laboratory: Cincinnati, OH, USA, 1997.
29. Milton, E. Review article principles of field spectroscopy. *Int. J. Remote Sens.* **1987**, *8*, 1807–1827. [CrossRef]
30. Mobley, C.D. Estimation of the remote-sensing reflectance from above-surface measurements. *Appl. Opt.* **1999**, *38*, 7442–7455. [CrossRef] [PubMed]
31. Vanhellemont, Q.; Ruddick, K. Atmospheric correction of metre-scale optical satellite data for inland and coastal water applications. *Remote Sens. Environ.* **2018**, *216*, 586–597. [CrossRef]
32. Vanhellemont, Q.; Ruddick, K. Atmospheric correction of Sentinel-3/OLCI data for mapping of suspended particulate matter and chlorophyll-a concentration in Belgian turbid coastal waters. *Remote Sens. Environ.* **2021**, *256*, 112284. [CrossRef]
33. Vanhellemont, Q. Adaptation of the dark spectrum fitting atmospheric correction for aquatic applications of the Landsat and Sentinel-2 archives. *Remote Sens. Environ.* **2019**, *225*, 175–192. [CrossRef]
34. Vanhellemont, Q. Daily metre-scale mapping of water turbidity using CubeSat imagery. *Opt. Express* **2019**, *27*, A1372–A1399. [CrossRef] [PubMed]
35. Vanhellemont, Q. Sensitivity analysis of the dark spectrum fitting atmospheric correction for metre-and decametre-scale satellite imagery using autonomous hyperspectral radiometry. *Opt. Express* **2020**, *28*, 29948–29965. [CrossRef]

36. De Keukelaere, L.; Sterckx, S.; Adriaensen, S.; Knaeps, E.; Reusen, I.; Giardino, C.; Bresciani, M.; Hunter, P.; Neil, C.; Van der Zande, D. Atmospheric correction of Landsat-8/OLI and Sentinel-2/MSI data using iCOR algorithm: Validation for coastal and inland waters. *Eur. J. Remote Sens.* **2018**, *51*, 525–542. [CrossRef]
37. Berk, A.; Anderson, G.P.; Acharya, P.K.; Bernstein, L.S.; Muratov, L.; Lee, J.; Fox, M.; Adler-Golden, S.M.; Chetwynd, J.H., Jr.; Hoke, M.L. MODTRAN5: 2006 update. In Proceedings of the Algorithms and Technologies for Multispectral, Hyperspectral, and Ultraspectral Imagery XII, Orlando, FL, USA, 17–20 April 2006; pp. 508–515.
38. Wolters, E.; Toté, C.; Sterckx, S.; Adriaensen, S.; Henocq, C.; Bruniquel, J.; Scifoni, S.; Dransfeld, S. iCOR Atmospheric correction on Sentinel-3/OLCI over land: Intercomparison with AERONET, RadCalNet, and SYN Level-2. *Remote Sens.* **2021**, *13*, 654. [CrossRef]
39. USGS. *Landsat 8-9 Collection 2 (C2) Level 2 Science Product (L2SP) Guide*; USGS: Sioux Falls, SD, USA, 2023; pp. 1–43.
40. Brockmann, C.; Doerffer, R.; Peters, M.; Kerstin, S.; Embacher, S.; Ruescas, A. Evolution of the C2RCC neural network for Sentinel 2 and 3 for the retrieval of ocean colour products in normal and extreme optically complex waters. In Proceedings of the Living Planet Symposium, Prague, Czech Republic, 9–13 May 2016; p. 54.
41. Soriano-González, J.; Urrego, E.P.; Sòria-Perpinyà, X.; Angelats, E.; Alcaraz, C.; Delegido, J.; Ruíz-Verdú, A.; Tenjo, C.; Vicente, E.; Moreno, J. Towards the combination of C2RCC processors for improving water quality retrieval in inland and coastal areas. *Remote Sens.* **2022**, *14*, 1124. [CrossRef]
42. Kyryliuk, D.; Kratzer, S. Evaluation of Sentinel-3A OLCI products derived using the Case-2 Regional CoastColour processor over the Baltic Sea. *Sensors* **2019**, *19*, 3609. Available online: https://www.mdpi.com/1424-8220/19/16/3609 (accessed on 15 February 2022). [CrossRef] [PubMed]
43. Schiller, H.; Doerffer, R. Neural network for emulation of an inverse model operational derivation of Case II water properties from MERIS data. *Int. J. Remote Sens.* **1999**, *20*, 1735–1746. [CrossRef]
44. Rodríguez-López, L.; Duran-Llacer, I.; Gonzalez-Rodriguez, L.; Abarca-del-Rio, R.; Cárdenas, R.; Parra, O.; Martinez-Retureta, R.; Urrutia, R. Spectral analysis using LANDSAT images to monitor the chlorophyll-a concentration in Lake Laja in Chile. *Ecol. Inform.* **2020**, *60*, 101183. [CrossRef]
45. Dang, X.; Du, J.; Wang, C.; Zhang, F.; Wu, L.; Liu, J.; Wang, Z.; Yang, X.; Wang, J. A Hybrid Chlorophyll a Estimation Method for Oligotrophic and Mesotrophic Reservoirs Based on Optical Water Classification. *Remote Sens.* **2023**, *15*, 2209. Available online: https://www.mdpi.com/2072-4292/15/8/2209 (accessed on 15 September 2023). [CrossRef]
46. Raynolds, M.K.; Comiso, J.C.; Walker, D.A.; Verbyla, D. Relationship between satellite-derived land surface temperatures, arctic vegetation types, and NDVI. *Remote Sens. Environ.* **2008**, *112*, 1884–1894. [CrossRef]
47. Gitelson, A.A.; Kaufman, Y.J.; Merzlyak, M.N. Use of a green channel in remote sensing of global vegetation from EOS-MODIS. *Remote Sens. Environ.* **1996**, *58*, 289–298. [CrossRef]
48. Bannari, A.; Khurshid, K.S.; Staenz, K.; Schwarz, J.W. A comparison of hyperspectral chlorophyll indices for wheat crop chlorophyll content estimation using laboratory reflectance measurements. *IEEE Trans. Geosci. Remote Sens.* **2007**, *45*, 3063–3074. [CrossRef]
49. Gitelson, A.A.; Gritz, Y.; Merzlyak, M.N. Relationships between leaf chlorophyll content and spectral reflectance and algorithms for non-destructive chlorophyll assessment in higher plant leaves. *J. Plant Physiol.* **2003**, *160*, 271–282. [CrossRef]
50. Gitelson, A.A.; Keydan, G.P.; Merzlyak, M.N. Three-band model for noninvasive estimation of chlorophyll, carotenoids, and anthocyanin contents in higher plant leaves. *Geophys. Res. Lett.* **2006**, *33*, L11402. [CrossRef]
51. Baughman, C.A.; Jones, B.M.; Bartz, K.K.; Young, D.B.; Zimmerman, C.E. Reconstructing turbidity in a glacially influenced lake using the Landsat TM and ETM+ surface reflectance climate data record archive, Lake Clark, Alaska. *Remote Sens.* **2015**, *7*, 13692–13710. [CrossRef]
52. Cui, M.; Sun, Y.; Huang, C.; Li, M. Water turbidity retrieval based on uav hyperspectral remote sensing. *Water* **2022**, *14*, 128. [CrossRef]
53. Yang, Z.; Reiter, M.; Munyei, N. Estimation of chlorophyll-a concentrations in diverse water bodies using ratio-based NIR/Red indices. *Remote Sens. Appl. Soc. Environ.* **2017**, *6*, 52–58. [CrossRef]
54. Johan, F.B.; Jafri, M.Z.B.M.; San, L.H.; Omar, W.M.W.; Ho, T.C. Chlorophyll a Concentration of Fresh Water Phytoplankton Analysed by Algorithmic based Spectroscopy. *J. Phys. Conf. Ser.* **2018**, *1083*, 012015. [CrossRef]
55. Silvoso, J.; Izaguirre, I.; Allende, L. Picoplankton structure in clear and turbid eutrophic shallow lakes: A seasonal study. *Limnologica* **2011**, *41*, 181–190. [CrossRef]
56. Asim, M.; Matsuoka, A.; Ellingsen, P.G.; Brekke, C.; Eltoft, T.; Blix, K. A new spectral harmonization algorithm for Landsat-8 and Sentinel-2 remote sensing reflectance products using machine learning: A case study for the Barents Sea (European Arctic). *IEEE Trans. Geosci. Remote Sens.* **2022**, *61*, 1–19. [CrossRef]
57. Pahlevan, N.; Smith, B.; Alikas, K.; Anstee, J.; Barbosa, C.; Binding, C.; Bresciani, M.; Cremella, B.; Giardino, C.; Gurlin, D. Simultaneous retrieval of selected optical water quality indicators from Landsat-8, Sentinel-2, and Sentinel-3. *Remote Sens. Environ.* **2022**, *270*, 112860. [CrossRef]
58. Smith, B.; Pahlevan, N.; Schalles, J.; Ruberg, S.; Errera, R.; Ma, R.; Giardino, C.; Bresciani, M.; Barbosa, C.; Moore, T. A chlorophyll-a algorithm for Landsat-8 based on mixture density networks. *Front. Remote Sens.* **2021**, *1*, 623678. [CrossRef]
59. Choo, Y.; Kang, G.; Kim, D.; Lee, S. A study on the evaluation of water-bloom using image processing. *Environ. Sci. Pollut. Res.* **2018**, *25*, 36775–36780. [CrossRef]

60. Guimarães, T.T.; Veronez, M.R.; Koste, E.C.; Gonzaga, L., Jr.; Bordin, F.; Inocencio, L.C.; Larocca, A.P.C.; De Oliveira, M.Z.; Vitti, D.C.; Mauad, F.F. An alternative method of spatial autocorrelation for chlorophyll detection in water bodies using remote sensing. *Sustainability* **2017**, *9*, 416. [CrossRef]
61. Kim, E.-J.; Nam, S.-H.; Koo, J.-W.; Hwang, T.-M. Hybrid approach of unmanned aerial vehicle and unmanned surface vehicle for assessment of chlorophyll-a imagery using spectral indices in stream, South Korea. *Water* **2021**, *13*, 1930. [CrossRef]